Supplementary Information

Phage capsid nanoparticles with defined ligand arrangement block influenza virus entry - An antiviral strategy

Daniel Lauster, Simon Klenk, Kai Ludwig, Saba Nojoumi, Sandra Behren, Lutz Adam, Marlena Stadtmüller, Sandra Saenger, Stephanie Franz, Katja Hönzke, Ling Yao, Ute Hoffmann, Markus Bardua, Alf Hamann, Martin Witzenrath, Leif E. Sander, Thorsten Wolff, Andreas C. Hocke, Stefan Hippenstiel, Sacha De Carlo, Jens Neudecker, Klaus Osterrieder, Nediljko Budisa, Roland R. Netz, Christoph Böttcher, Susanne Liese,* Andreas Herrmann,* Christian P. R. Hackenberger*

Table of contents

1 Supplementary Figures

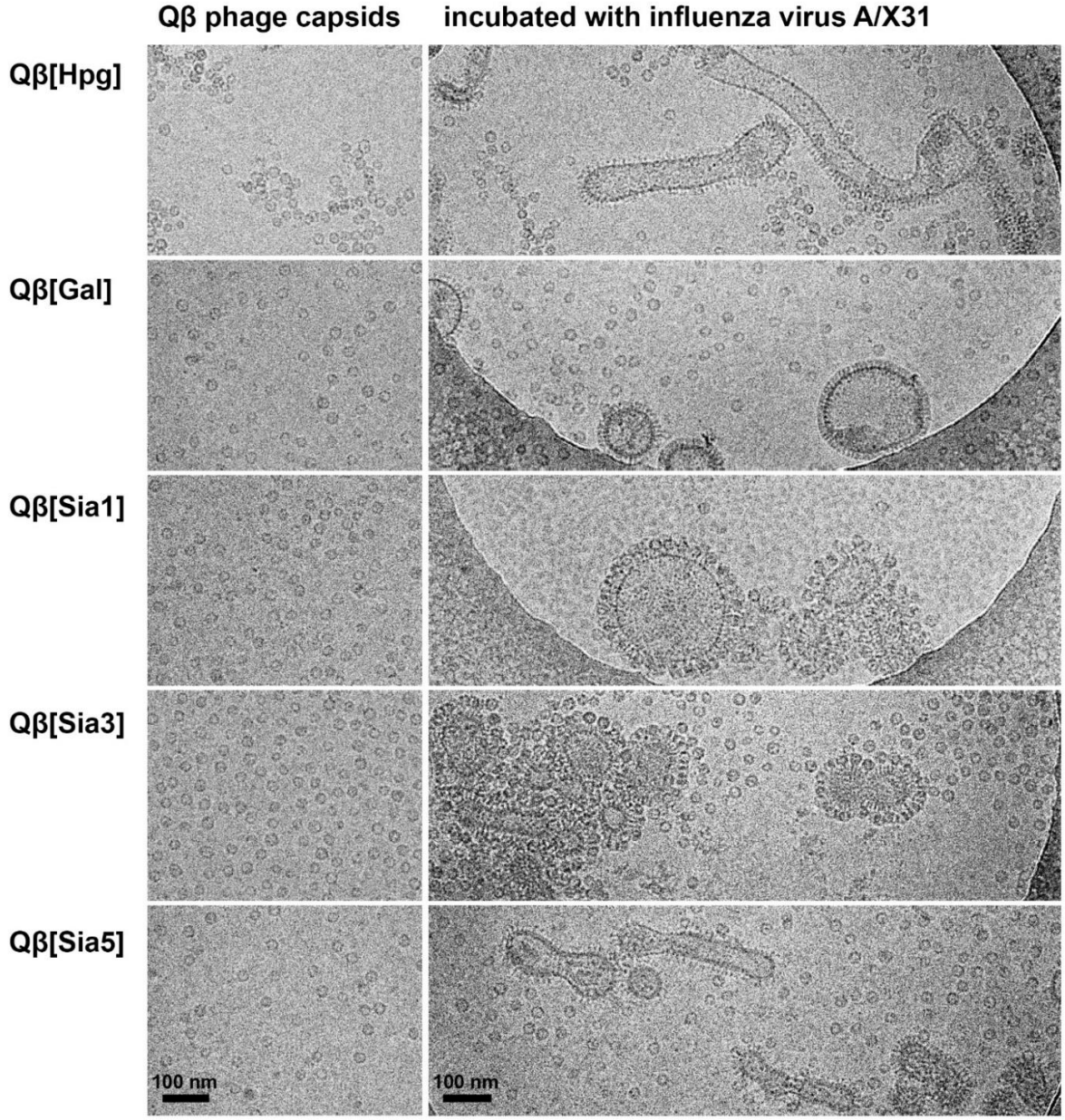

Supplementary Figure 1: Cryo-Transmission Electron Microscopy. Cryo-micrographs of the various Qβ phage capsids (left) and incubated with influenza virus A/X31 (right).

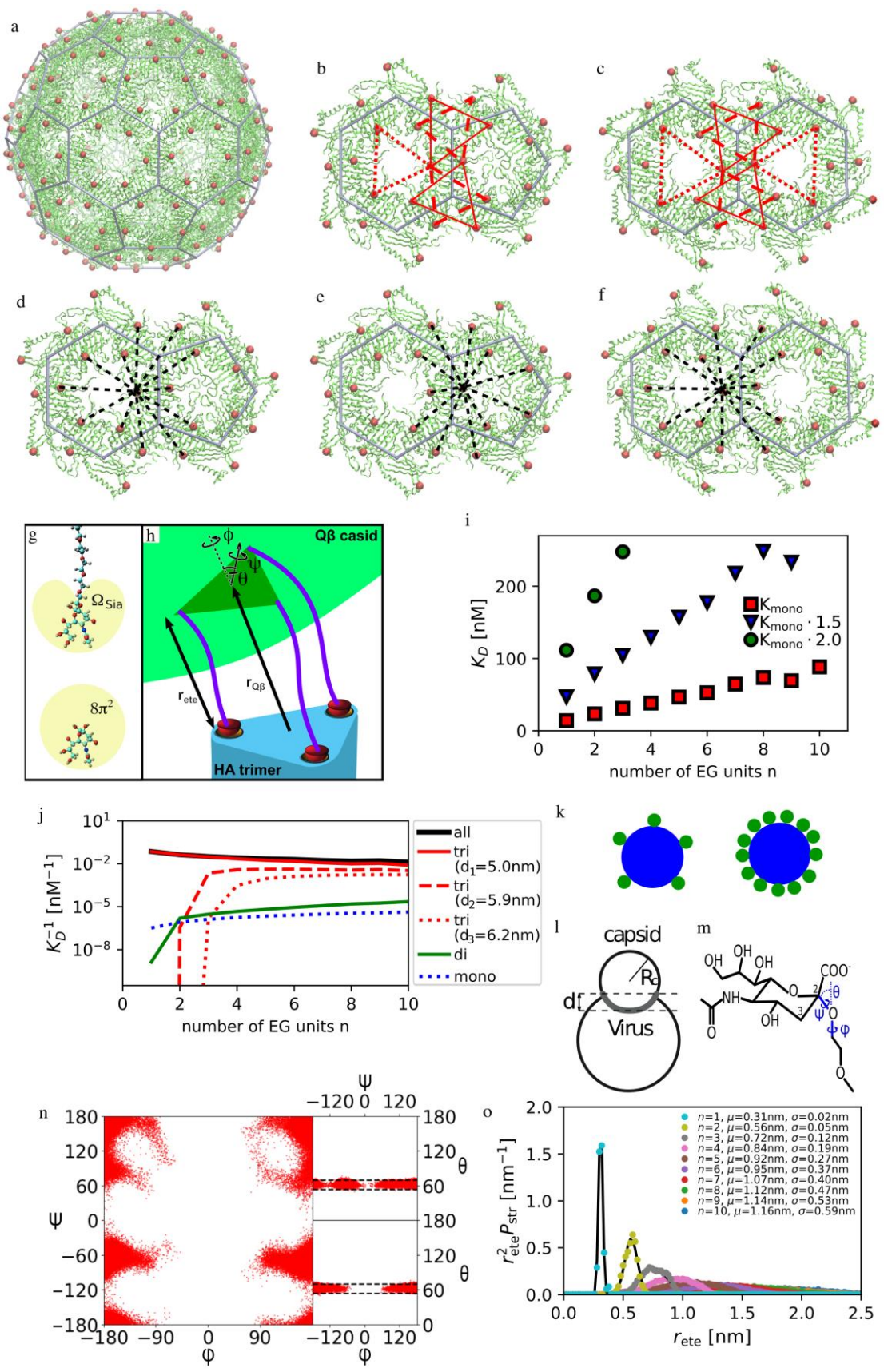

Supplementary Figure 2: (**a**) Crystal structure (pdb: 1qbe) of a Qβ capsid. The hexagon and pentagon substructures are indicated as gray lines. The anchoring points of the Sia units are shown as red points. (**b**) Sia triplets in a hexagon-pentagon substructure. (**c**) Sia triplets

in a hexagon-hexagon substructure. (**d**) Sia duplets in a hexagon-pentagon substructure, whereby the initial Sia is found in the hexagon substructure. (**e**) Sia duplets in a hexagon-pentagon structure, whereby the initial Sia is found in the pentagon substructure. (**f**) Sia duplets in a hexagon-hexagon substructure. (**g**) An unbound monovalent Sia (bottom) can freely rotate around all axes in space, which leads to an angular space of $8\pi^2$. The steric restrictions due to the presence of the EG linker (top) reduce the angular space to Ω_{Sia}. (**h**) Schematic picture of the position and orientation of the Qβ capsid. The vector $r_{Q\beta}$ denotes the position of the Qβ capsid (green) relative to the HA trimer (blue), while the capsid orientation is quantified by the Euler angles ϕ,θ,ψ. The Sia units are indicated as red half spheres and the EG linkers as purple lines. (**i**) Dissociation constant (**Eq.11**) for varying K_{mono}. The cooperativity factor C_3 as well as the angular restriction factor ω_{sia} are the same in all three cases. (**j**) The inverse of the dissociation constant (**Eq. 10**) is shown together with the contribution from mono-, di- and trivalently bound Qβ capsids. The edge lengths (d_1, d_2 and d_3) of the Sia triplets are indicated in the legend. (**k**) Illustration of the arrangement of Qβ capsids on the virus surface for the minimal (left) and maximal (right) number of capsids per virus. (**l**) Schematic picture of the contact between a deformable virus and a spherical Qβ capsid. (**m**) Illustration of the Euler angles at the connection between the Sia unit and the EG linker. (**n**) Scatterplot of the Euler angles from an MD simulation of a Sia unit connected to an EG linker in water. (**o**) The stretching probability P_{str}, obtained from MD simulations, of all ten EG oligomers is shown in dependence of the end-to-end distance $\boldsymbol{r_{ete}}$.

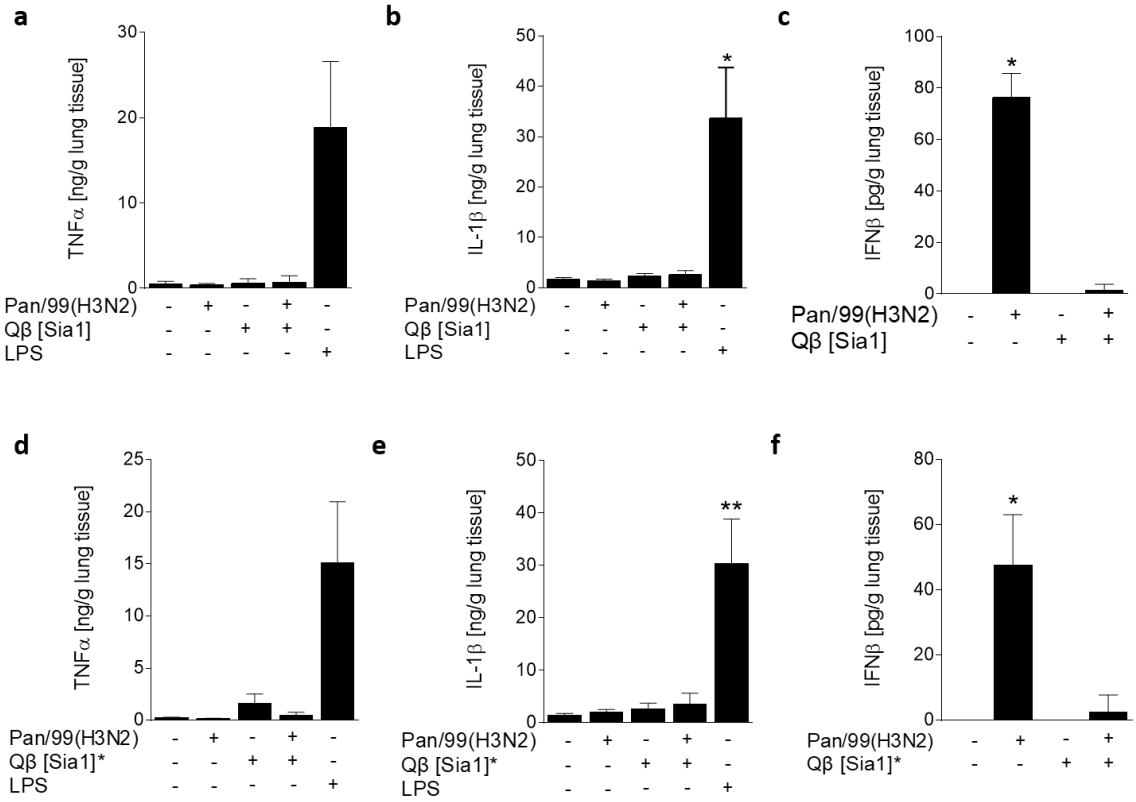

Supplementary Figure 3. Human lung tissue infection experiments and production of TNF-α, IL1-β and IFNβ. Experiments were conducted either with Qβ capsids, which were purified in a standard procedure (a-c) or additionally purified capsids (indicated with *) using an endotoxin removal procedure (d-f). For 10 nM Qβ[Sia1], as used in the lung experiments, 8,08±0.18 endotoxin units per milliliter (EU/ml) were measured with an endotoxin detection

assay for phage capsids from a standard purification, and no endotoxin could be detected after endotoxin removal (detection limit <1 EU/ml). 1 EU/ml corresponds to 0.1-0.2 ng/ml LPS equivalents. LPS (10 ng/ml) was used as positive control for the stimulation of innate immunity. Cytokine levels were measured using an ELISA 48 h after stimulation of tissue with the indicated materials. Error bars represent the S.D. (N=4). For statistical analysis a two-tailed Mann-Whitney test was conducted (*=p<0.05, **=p<0.005).

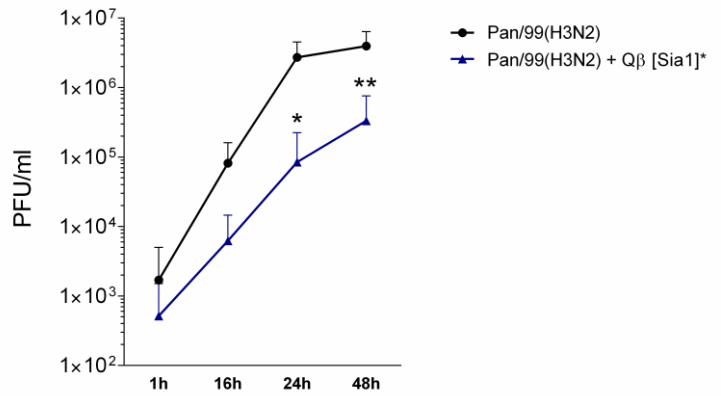

Supplementary Figure 4. Human lung tissue infection experiments with Pan/99 (H3N2) and treatment with 10 nM endotoxin-free Qβ-phage capsids Qβ[Sia1]*. Error bars indicate the S.D. (N=4). For statistical analysis a two-tailed Mann-Whitney test was conducted (*=p<0.05, **=p<0.005).

2 Experimental Section

2.1 NMR spectroscopy

^{1}H- and ^{13}C-NMR spectra were recorded on a Bruker Avance 300 (300 MHz) and Avance 600 (600 MHz) NMR spectrometer. Measurements were done at room temperature (rt), and chemical shifts are reported in parts per million (ppm) relative to the residual solvent peaks[33]. Coupling constants J are reported in Hz and multiplicities are given as s = singlet, br s = broad singlet, d = doublet, t = triplet, q = quadruplet, m = multiplet, and corresponding combinations of these.

2.2 High resolution mass spectrometry of small molecules

High resolution ESI-MS spectra were recorded on an Agilent 6220 TOF Accurate Mass coupled to an Agilent 1200 LC and were measured at 35°C between 100 – 2000 m/z. The used column was an Accucore RP-MS (30 x 2.11 mm; 2.66 µm particle size) ran with a flow of 0.8 mL/min and the following gradient (A = water, B = acetonitrile): 95% A + 5% B for 0.2 min, then 95% A + 5% B to 1% A + 99% B until 1.1 min, then 1% A + 99% B until 2.5 min.

2.3 Material and reagents

Column chromatography was performed with silica gel NORMASIL 60 (40–63 µm). For thin-layer chromatography (TLC) glass-backed silica gel plates (60 F254, 0.2 mm, Merck, Darmstadt, Germany) were used and detected either by UV or stained with anisaldehyde solution (112.5 mL methanol, 15 mL acetic acid, 7.5 mL H_2SO_4, 0.75 mL anisaldehyde) or potassium permanganate solution (1.5 g of $KMnO_4$, 10 g K_2CO_3, 1.25 mL 10% NaOH, 200 mL water).

Acidic resin for ion-exchange (DOWEX®-50WX4) was washed extensively with methanol prior to use.

Air and moist sensitive reactions were performed under an atmosphere of argon in flame-dried Schlenk flasks. Dry solvents were obtained by Acros Organics. All other solvents and reagents were purchased from commercial suppliers as reagent grade and used without further purification.

2.4 Syntheses of linkers and TEOTA ligand

The linker compounds 2-azidoethanol (mEG-N_3) **1**[34], 2-[2-(2-azidoethoxy)ethoxy]ethanol (tEG-N_3) **2**[35], 2-(2-(2-(2-(2-azidoethoxy)ethoxy)ethoxy)ethoxy)ethanol (pEG-N_3) **3**[36] and 1-azido-23-hydroxy-3,6,9,12,15,18,21-heptaoxatricosane (oEG-N_3) **4**[37], as well as the copper-chelating ligand TEOTA[38] were synthesized according to published protocols.

2.5 Sialic acid donor synthesis

Methyl ester **6** and peracetylated sialic acid **7** were synthesized according to a literature procedure by microwave assistance starting from commercially available *N*-acetylneuraminic acid **5**[39]. The following steps towards fully protected thiosialoside donor **10** were performed according to a protocol published by Crich and coworkers[30]:

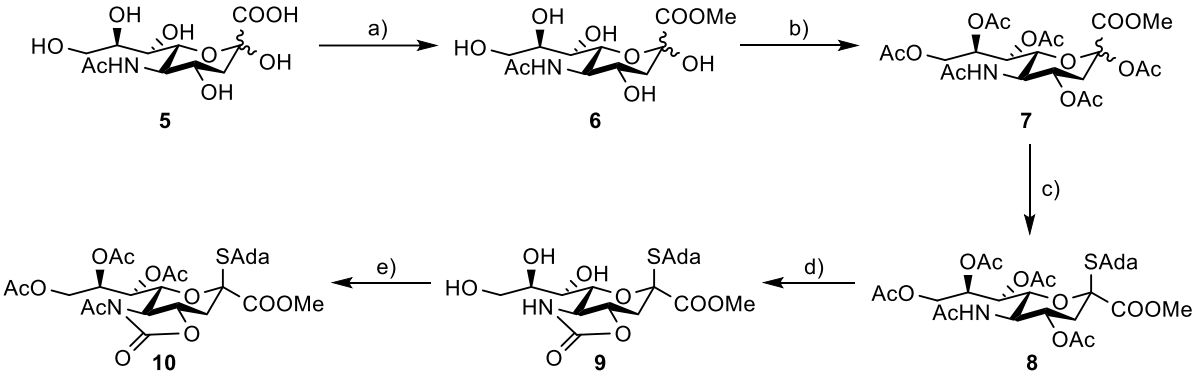

Scheme S 1: Synthetic route towards oxazolidinione protected sialyl donor **10**. Conditions: a) methanol. cat. trifluoroacetic acid, µwave, 80°C, 30 min; b) *N*,*N*-dimethylaminopyridine, pyridine, acetic anhydride, µwave, 70°C, 10 min; c) boron trifluoride etherate, 1-adamantanethiol, dichloromethane, 0°C to room temperature, 1 d; d) 1.) methanesulfonic acid, methanol, 70°C, 1 d, 2.) 4-nitrophenyl chloroformate, sodium bicarbonate, water/acetonitrile 1:1, 0°C, 3 h; e) 1.) pyridine, acetic anhydride, room temperature, 14 h, 2.) acetyl chloride, *N*,*N*-diisopropylethylamine, 0°C to room temperature, 2 h.

Sialic acid chloride **11** was synthesized according a published protocol using peracetylated sialic acid **7**[40]:

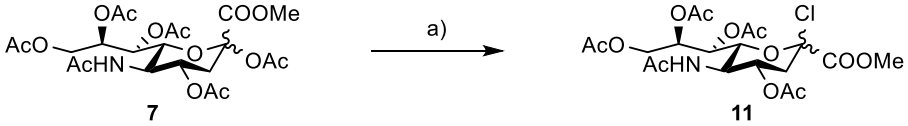

Scheme S 2: Synthesis of sialic acid chloride **11**. Conditions: a) anhydrous methanol, hydrochloric acid, acetyl chloride, 0°C, 12 h.

2.6 Syntheses of sialic acid azides

Methyl [5-Acetamido-3,5-dideoxy-4,7,8,9-tetra-*O*-acetyl-2-azido-D-glycero-α-D-galacto-non-2-ulopyranoside]onate (**AcSia0-N$_3$**) was synthesized from sialic acid chloride **11** according to a literature protocol[41].

The trisaccharides 2,3- and 2,6-sialyllactose azides were synthesized according to a previously published protocol[42]. The spectrometric data are in accordance with those given in the respective literature.

2,3-Sialyllactose azide **2.3SL**:

ESI-HR-MS calculated for $C_{23}H_{38}N_4O_{18}K^+$: m/z = 697.1818, found: m/z = 697.1817.

2,6-Sialyllactose azide **2.6SL**:

ESI-HR-MS calculated for $C_{23}H_{38}N_4O_{18}H^+$: m/z = 659.2259, found: m/z = 659.2254.

2.7 General glycosylation method

Glycosylations of the sialic acid donor with corresponding linker-azides were performed according to the literature protocol[30]. In a Schlenk flask powdered molecular sieves 4 Å were evacuated, heated and flooded with argon three times. Subsequently, sialic acid donor **10** (1.0 equiv.) and the corresponding linker **1** - **4** (1.5 equiv.) were added, evacuated for 15 min and then dissolved in dry CH_2Cl_2/MeCN (1:1, 0.05 mL per mg donor). The solution was stirred for 1 h at room temperature under argon and was then cooled down to –78 °C (dry ice/acetone bath) followed by the addition of *N*-iodosuccinimide (2.4 equiv.) and triflic acid (1.0 equiv.). The reaction was stirred for at least 1 h before it was quenched with triethylamine (1.5 equiv.) and then filtered through Celite® with CH_2Cl_2, washed with 20% aq. $Na_2S_2O_3$ solution, dried over $MgSO_4$ and at finally concentrated under reduced pressure. Purification was performed by column chromatography.

2.8 General deprotection method

Glycosylated azido sugars were dissolved in MeOH (0.05 mL per mg protected sugar). To the solution 1 M aqueous NaOH (0.015 mL per mg protected sugar) was added and stirred at room temperature for 30 min. Complete conversion was verified by TLC (EtOAc). The mixture was neutralized by the addition of DOWEX®-50WX4 H^+ resin, filtered, concentrated under reduced pressure und finally lyophilized to provide the corresponding unprotected azido sugars.

2.8.1 [5-Acetamido-3,5-dideoxy-2-azido-D-glycero-α-D-galacto-non-2-ulopyranoside]onate (Sia0)

Deprotection of **AcSia0-N_3** according to the general deprotection method led to **Sia0-N_3** as colorless solid (64.0 mg, 0.20 mmol, quant.).

^{1}H-NMR (300 MHz, D_2O): δ = 1.65 (t, *J* = 12.0 Hz, 1H, 3-H_{ax}), 1.98 (s, 3H, NAc), 2.61 (dd, *J* = 12.9, 4.1 Hz, 1H, 3-H_{eq}), 3.50-3.66 (m, 3H), 3.75-3.88 (m, 4H).

^{13}C-NMR (75 MHz, D_2O): δ = 21.9, 38.1, 51.4, 62.7, 67.3, 68.0, 70.6, 73.7, 89.4, 170.6, 174.9.

ESI-HR-MS calculated for $C_{11}H_{19}N_4O_8^+$: *m/z* = 335.1203; found: *m/z* = 335.1197.

2.8.2 Methyl-((2-azido)ethyl-5-acetamido-7,8,9-tri-*O*-acetyl-5-*N*,4-*O*-carbonyl-3,5-dideoxy-D-glycero-α-D-galacto-non-2-ulopyranoside)onate (AcSia1)

By using linker **1** with the general glycosylation method, **AcSia1-N_3** was obtained after column chromatography (Hex/EtOAc 2:1 → 1:1) as light yellow oil (132 mg, 0.24 mmol, 76%).

^{1}H-NMR (300 MHz, $CDCl_3$): δ = 2.01-2.04 (m, 4H, OAc, 3-H_{ax}), 2.12, 2.13 (2x s, 6H, 2x OAc), 2.48 (s, 3H, NAc), 2.87 (dd, *J* = 12.2, 3.5 Hz, 1H, 3-H_{eq}), 3.36 (t, *J* = 4.8 Hz, 2H, CH_2N_3), 3.40-3.48 (m, 1H), 3.50-3.61 (m, 1H), 3.69-3.80 (m, 1H), 3.81 (s, 3H, COOMe), 3.96-4.08 (m, 2H), 4.37 (dd, *J* = 12.3, 2.8 Hz, 1H), 4.61-4.68 (m, 1H), 5.39-5.48 (m, 1H), 5.56-5.64 (m, 1H).

^{13}C-NMR (75 MHz, $CDCl_3$): δ = 20.9, 21.2, 21.3, 24.8, 36.7, 50.6, 53.2, 59.1, 63.3, 64.9, 68.9, 71.7, 74.9, 75.8, 99.1, 153.7, 168.8, 170.2, 170.3, 170.8, 172.1.

ESI-HR-MS calculated for $C_{21}H_{29}N_4O_{13}^+$: *m/z* = 545.1726; found: *m/z* = 545.1725.

2.8.3 (2-Azidoethyl)-5-acetamido-3,5-dideoxy-D-glycero-α-D-galacto-non-2-ulopyranosidic acid (Sia1)

Deprotection of **AcSia1-N_3** according to the general deprotection method led to **Sia1-N_3** as colorless gel (70.5 mg, 0.19 mmol, 85%).

^{1}H-NMR (300 MHz, D_2O): δ = 1.76 (t, *J* = 12.1 Hz, 1H, 3-H_{ax}), 2.00 (s, 3H, NAc), 2.70 (dd, *J* = 12.6, 4.4 Hz, 1H, 3-H_{eq}), 3.46 (t, *J* = 4.9 Hz, 2H, CH_2N_3), 3.61-3.97 (m, 9H).

^{13}C-NMR (75 MHz, D_2O): δ = 21.9, 39.2, 50.2, 51.6, 62.7, 63.0, 67.5, 68.1, 70.9, 72.7, 99.2, 171.5, 174.9.

ESI-HR-MS calculated for $C_{13}H_{21}N_4O_9^-$: *m/z* = 377.1314; found: *m/z* = 377.1302.

2.8.4 Methyl-((2-(2-azidoethoxy)ethoxy)ethyl-5-acetamido-7,8,9-tri-*O*-acetyl-5-*N*,4-*O*-carbonyl-3,5-dideoxy-D-glycero-α-D-galacto-non-2-ulopyranoside)onate (AcSia3)

By using linker **2** with the general glycosylation method, **AcSia3-N_3** was obtained after column chromatography (Hex/EtOAc 1:1 → 100% EtOAc) as light yellow oil (100 mg, 0.16 mmol, 93%).

^{1}H-NMR (300 MHz, $CDCl_3$): δ = 2.03 (s, 3H, Ac), 2.09-2.19 (m, 1H, 3-H_{ax}) 2.13, 2.14 (2x s, 6H, OAc), 2.49 (s, 3H, NAc), 2.89 (dd, *J* = 12.1, 3.5 Hz, 1H, 3-H_{eq}), 3.39 (t, *J* = 5.1 Hz, 2H, CH_2N_3), 3.45-3.55 (m, 1H), 3.59-3.72 (m, 9H), 3.80 (s, 3H, $COOCH_3$), 3.89-4.10 (m, 3H), 4.37 (dd, *J* = 12.3, 2.8 Hz, 1H), 4.61 (dd, *J* = 9.3, 1.6 Hz, 1H), 5.37-5.46 (m, 1H), 5.57 (dd, *J* = 8.0, 1.6 Hz, 1H).

^{13}C-NMR (75 MHz, $CDCl_3$): δ = 20.8, 21.0, 21.2, 24.7, 36.5, 50.7, 53.0, 59.0, 63.1, 65.1, 69.1, 70.0, 70.2, 70.5, 70.7, 71.8, 75.0, 75.5, 99.3, 153.8, 168.7, 170.1, 170.3, 170.7, 172.1.

ESI-HR-MS calculated for $C_{25}H_{36}N_4O_{15}Na^+$: *m/z* = 655.2069; found: *m/z* = 655.2048.

2.8.5 (2-(2-(2-Azidoethoxy)ethoxy)ethyl)-5-acetamido-3,5-dideoxy-D-glycero-α-D-galacto-non-2-ulopyranosidic acid (Sia3)

Deprotection of **AcSia1-N_3** according to the general deprotection method led to **Sia3-N_3** as light yellow solid (71.0 mg, 0.15 mmol, 95%).

^{1}H-NMR (300 MHz, D_2O): δ = 1.65 (t, *J* = 12.1 Hz, 1H, 3-H_{ax}), 2.01 (s, 3H, NHAc), 2.71 (dd, *J* = 12.5, 4.5 Hz, 1H, 3-H_{eq}), 3.48 (t, *J* = 4.9 Hz, 2H, CH_2N_3), 3.53 – 3.60 (m, 2H), 3.63 – 3.72 (m, 10H), 3.75-3.92 (m, 5H).

^{13}C-NMR (75 MHz, D_2O): δ = 21.9, 39.3, 50.0, 51.6, 62.7, 63.2, 67.5, 68.1, 69.1, 69.29, 69.32, 69.4, 70.9, 72.6, 99.1, 171.6, 174.8.

ESI-HR-MS calculated for $C_{17}H_{29}N_4O_{11}^-$: *m/z* = 465.1838; found: *m/z* = 465.1841.

2.8.6 Methyl-((2-(2-(2-(2-azidoethoxy)ethoxy)ethoxy)ethyl-5-acetamido-7,8,9-tri-*O*-acetyl-5-*N*,4-*O*-carbonyl-3,5-dideoxy-D-glycero-α-D-galacto-non-2-ulopyranoside)-onate (AcSia5)

By using linker **3** with the general glycosylation method, **AcSia5-N_3** was obtained after column chromatography (Hex/EtOAc 1:1 -→ 100% EtOAc) as light yellow oil (212 mg, 0.29 mmol, 91%).

^{1}H-NMR (300 MHz, $CDCl_3$): δ = 2.00-2.04 (m, 4H, OAc, 3-H_{ax}), 2.12, 2.13 (2x s, 6H, 2x OAc), 2.48 (s, 3H, NAc), 2.88 (dd, *J* = 12.1, 3.5 Hz, 1H, 3-H_{eq}), 3.38 (t, *J* = 5.0 Hz, 2H, CH_2N_3), 3.43-3.52 (m, 1H), 3.60-3.69 (m, 17H), 3.79 (s, 3H, COOMe), 3.87-4.07 (m, 3H), 4.35 (dd, *J* = 12.3, 2.9 Hz, 1H), 4.59 (dd, *J* = 9.3, 1.6 Hz, 1H), 5.35-5.45 (m, 1H), 5.56 (dd, *J* = 8.0, 1.6 Hz, 1H).

^{13}C-NMR (75 MHz, $CDCl_3$): δ = 20.9, 21.1, 21.3, 24.8, 36.6, 50.8, 53.1, 59.1, 63.2, 65.2, 69.1, 70.1, 70.2, 70.59, 70.64, 70.68, 70.73, 70.77, 70.8, 71.9, 75.1, 75.6, 99.4, 153.8, 168.8, 170.2, 170.3, 170.8, 172.1.

ESI-HR-MS calculated for $C_{29}H_{44}N_4O_{17}Na^+$: *m/z* = 743.2594; found: *m/z* = 743.2546.

2.8.7 (2-(2-(2-(2-(2-Azidoethoxy)ethoxy)ethoxy)ethoxy)ethyl)-5-acetamido-3,5-dideoxy-D-glycero-α-D-galacto-non-2-ulopyranosidic acid (Sia5)

Deprotection of **AcSia5-N$_3$** according to the general deprotection method led to **Sia5-N$_3$** as yellow oil (123 mg, 0.22 mmol, 79%).

^{1}H-NMR (300 MHz, D_2O): δ = 1.75 (t, *J* = 12.1 Hz, 1H, 3-H_{ax}), 2.00 (s, 3H, NAc), 2.69 (dd, *J* = 12.7, 4.4 Hz, 1H, 3-H_{eq}), 3.48 (t, *J* = 4.9 Hz, 2H, CH_2N_3), 3.56-3.76 (m, 20H), 3.77-3.88 (m, 4H), 3.88-3.97 (m, 1H).

^{13}C-NMR (75 MHz, D_2O): δ = 21.9, 39.3, 50.0, 51.6, 62.7, 63.1, 67.4, 68.1, 69.1, 69.3, 69.38, 69.4, 69.5, 70.9, 71.6, 72.6, 99.1, 171.6, 174.8.

ESI-HR-MS calculated for $C_{21}H_{37}N_4O_{13}^-$: *m/z* = 553.2363; found: *m/z* = 553.2358.

2.8.8 Methyl-((2-(2-(2-(2-(2-(2-(2-azidoethoxy)ethoxy)ethoxy)ethoxy)ethoxy)ethoxy)ethyl)-5-acetamido-7,8,9-tri-*O*-acetyl-5-*N*,4-*O*-carbonyl-3,5-dideoxy-D-glycero-α-D-galacto-non-2-ulopyranoside)-onate (AcSia8)

By using linker **4** with the general glycosylation method, **AcSia8-N$_3$** was obtained after preparative HPLC (C18, H_2O/MeCN 95:5 → 10:90 in 60 min) and lyophilization as yellow thick oil (74.2 mg, 87.0 µmol, 58%).

^{1}H-NMR (300 MHz, $CDCl_3$): δ = 1.87 (s, 3H), 1.97 (t, *J* = 12.7 Hz, 1H), 2.02, 2.03, 2.13, 2.14 (4 x s, 3H each), 2.60 (dd, *J* = 12.8, 4.6 Hz, 1H), 3.38 (t, *J* = 5.1 Hz, 2H), 3.41-3.49 (m, 1H), 3.58-3.70 (bm, 28H), 3.79 (s, 3H), 3.84-3.93 (m, 1H), 4.01-4.13 (m, 3H), 4.28 (dd, *J* = 12.4, 2.6 , Hz, 1H), 4.77-4.91 (m, 1H), 5.09-5.20 (m, 1H), 5.27-5.34 (m, 1H), 5.34-5.42 (m, 1H) ppm.

^{13}C-NMR (75 MHz, $CDCl_3$): δ = 20.8, 20.89, 20.92, 21.2, 23.2, 38.0, 49.4, 50.7, 52.8, 62.4, 64.5, 67.3, 68.6, 69.2, 70.06, 70.1, 70.5, 70.57, 70.59, 70.60, 70.65, 70.69, 70.72, 72.5, 98.8, 168.3, 170.1, 170.2, 170.3, 170.7, 171.1 ppm.

ESI-HR-MS calculated for $C_{36}H_{60}N_4O_{20}H^+$: m/z = 869.3874, found: m/z = 869.3870.

2.8.9 (2-(2-(2-(2-(2-(2-(2-(2-Azidoethoxy)ethoxy)ethoxy)ethoxy)ethoxy)ethoxy)ethoxy)-ethyl)-5-acetamido-3,5-dideoxy-D-glycero-α-D-galacto-non-2-ulopyranosidic acid (Sia8)

Deprotection of **AcSia8-N$_3$** according to the general deprotection method led to **Sia8-N$_3$** as colorless solid (20.9 mg, 30.4 µmol, 91 %).

^{1}H-NMR (300 MHz, $CDCl_3$): δ = 1.65 (t, *J* = 12.1 Hz, 1H, 3-H_{ax}), 2.01 (s, 3H, NAc), 2.72 (dd, *J* = 12.4, 4.5 Hz, 1H, 3-H_{eq}), 3.48 (t, *J* =4.8 Hz, 2H, CH_2N_3), 3.52-3.60 (m, 3H), 3.63-3.79 (m, 30H), 3.79-3.94 (m, 4H) ppm.

^{13}C-NMR (75 MHz, $CDCl_3$): δ = 21.9, 40.1, 50.0, 51.7, 62.5, 63.1, 68.1, 69.1, 69.3, 69.37, 69.42, 71.6, 72.4, 100.4, 173.3, 174.9 ppm.

ESI-HR-MS calculated for $C_{27}H_{50}N_4O_{16}Na^+$: m/z = 709.3120, found: m/z = 709.3116.

2.9 Synthesis of GalNAc azide Gal3

Peracetylated galactosamine **13**[43], oxazoline **14**[44] and protected GalNAc azide **AcGal3**[45] were synthesized according to literature protocols starting from commercially available galactosamine hydrochloride **12**:

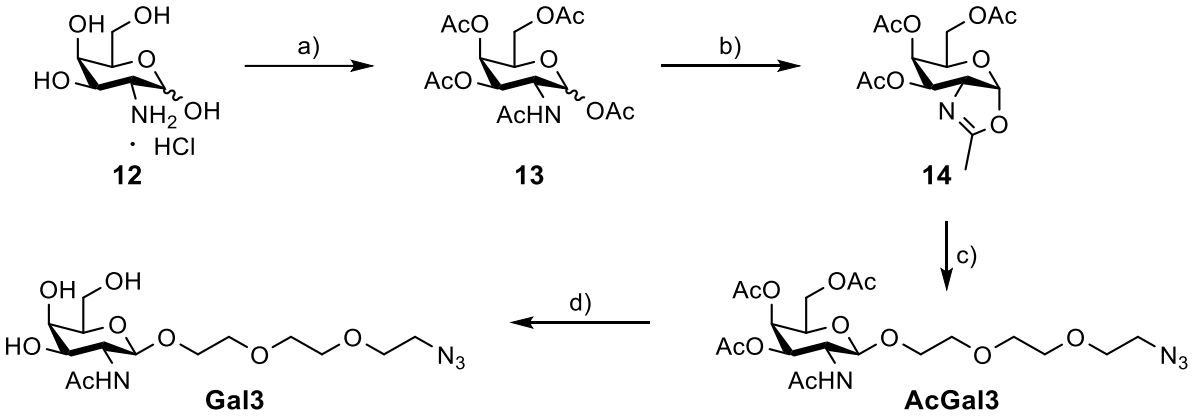

Scheme S 3: Synthetic route towards galactose derivative **Gal3**$_3$. Conditions: a) pyridine, acetic anhydride, 0°C to room temperature, 18 h; b) trimethylsilyl trifluoromethanesulfonate, 1,2-dichloroethane, 50°C, 17 h; c) trimethylsilyl trifluoromethanesulfonate, 1,2-dichloroethane, 4Å molecular sieves, room temperature, 12 h; d) 1 M sodium hydroxide, methanol, room temperature, 30 min.

2.9.1 2-[2-(2-azidoethoxy)ethoxy]ethoxy-2-*N*-acetylamido-2-deoxy-β-D-galacto-pyranoside Gal3

Deprotection of **AcGal3-N$_3$** according to the general deprotection method led to **Gal3-N$_3$** as pale yellow gel (515 mg, 1.36 mmol, quant.).

^{1}H-NMR (300 MHz, D_2O): δ = 2.02 (s, 3H, NHAc), 3.48 (t, *J* = 5.1 Hz, 2H, CH_2N_3), 3.62-3.79 (m, 13H), 3.83- 3.93 (m, 2H), 3.95-4.04 (m, 1H), 4.48 (d, *J* = 8.4 Hz, 1H, 1-H).

^{13}C-NMR (75 MHz, D_2O): δ = 22.1, 50.0, 52.2, 60.8, 67.7, 68.7, 69.1, 69.4, 69.5, 69.6, 71.0, 75.0, 101.4, 174.6.

ESI-HR-MS calculated for $C_{14}H_{26}N_4O_8Na^+$: *m/z* = 401.1648; found: *m/z* = 401.1649.

2.10 Generation of *E. coli* B834(pQE60_Qβ(K16M), pREP4)

E. coli B834 (DE3) was chosen as expression host for the Qβ(K16M) mutant as previously reported by the Davis lab[25]. Electrocompetent host cells were double-transformed with the circular nucleic acids pQE60_Qβ(K16M) and pREP4 (kindly provided by A. K. Udit, Occidental College, LA, CA)[29] carrying the antibiotic resistance cassettes ampicillin and kanamycin, respectively. The double transformation was performed in an electroporator with

a pulse of 1.8 kV. Transformed cells were cured in Luria-Bertani (LB) medium at 37 °C and subsequently incubated on LB-agar plates at 37 °C overnight.

2.11 Recombinant Qβ(K16HPG) expression and purification

New minimal media (NMM) was used to cultivate and express Qβ(K16M) virus like particles at all times.

A preculture of *E. coli* B834(pQE60_Qβ(K16M), pREP4) was prepared in 5 mL NMM supplemented with kanamycin (50 mg/L) and ampicillin (100 mg/L), which was subsequently incubated at 37 °C, 200 rpm for 8 h. 1-2 L NMM substituted with kanamycin (50 mg/L), ampicillin (100 mg/L) and L-methionine (130 mM) were inoculated with 6 mL of preculture. The resulting main culture was incubated at 30 °C, 180 rpm overnight (18 h). Subsequently, the culture was washed twice with NMM supplemented with kanamycin (50 mg/L) and ampicillin (100 mg/L) lacking L-methionine (400 rpm, 4 °C, 20 min)) twice. Washed culture pellets were resuspended in minimal media supplemented with kanamycin (50 mg/L), ampicillin (100 mg/L), and the resulting suspension was brought to half the cultivation volume in preheated NMM supplemented with kanamycin (50 mg/L), ampicillin (100 mg/L) at 30 °C. The ncAA HPG (L-homopropargylglycine) was added to the culture (50 mg/L). The expression culture was incubated at 37 °C, 180 rpm for 30 min. Subsequently, the culture was incubated at 30 °C, 180 rpm for 1 h. Expression of Qβ(K16M) was induced with IPTG (1 mM) followed by an incubation at 30 °C, 180 rpm, overnight (18 h). Cells were harvested (8,000 x g, 4 °C, 20 min) and stored at -20 °C until purification.

Cell pellets were thawed and resuspended in lysis buffer (100 mM potassium phosphate, pH 7.3) and lysed by ten passes through an LM10 microfluidizer (Microfluidics, Westwood, Massachusetts) at 14,000 psi. The resulting slurry was incubated with DNaseI in the presence of 10 mM $MgCl_2$ at room temperature for 30 min, and subsequently centrifuged to remove cell debris (50,000 x g, 20 min, 4 °C). To the supernatant 10% (w/v) PEG8000 and NaCl (100 mM final concentration) was added, and incubated overnight at 4 °C. The precipitate was collected by centrifugation (10,000 rpm, 15 min, 4 °C) and dissolved in 100 mM potassium phosphate buffer (pH 7.3). Extraction with $CHCl_3$/nBuOH (1:1) was carried out and phase separation as well as removal of insoluble material was achieved by centrifugation (10,000 rpm, 15 min, 4 °C). The resulting Qβ[Hpg] capsid containing supernatant was stored at 4 °C. Further purification was achieved by sucrose gradient (10-40% (w/v)) ultracentrifugation in an Optima LE-80K ultracentrifuge (Beckman Coulter) with an SW 40 Ti rotor (125,000 x g, 4.5 h, 4 °C). Qβ[Hpg] containing fractions were identified by SDS-PAGE, pooled, concentrated and washed in 30 kDa cut-off centrifugal filter units.

2.12 Determination of Qβ VLP concentration

Concentrations of Qβ containing solutions were measured by commercially an available Pierce™ BCA Protein Assay Kit (catalogue number 23225) using a BSA standard for calibration. Evaluation of the assay results were carried out by using the software Mathematica (Wolfram Research, Inc., Version 10.2, Champaign, IL).

2.13 ESI mass analysis of Qβ coat protein

Reaction progress and final products of conjugation reactions were analyzed by LC-ESI-MS. For that, 8 µL of capsid solution (23 – 177 µM of protein) were treated with 2 µL of 1 M TCEP and 4 µL of this mixture were injected into an Acquity UPLC (Waters

Corporation) equipped with a Waters Acquity UPLC Protein BEH C_4 300 Å column using water (A) and acetonitrile (B) as eluent which both contained 0.1% formic acid (95% A isocratic for 2.5 min, then gradient to 100% B in 7.5 min). The UPLC was coupled to an LCT Premier Micromass Technologies spectrometer operated at 3.2 kV capillary voltage, 60 V cone voltage, 300 °C desolvation temperature, 150 °C source temperature and 600 L/h desolvation gas. The obtained data were processed by MassLynx software (4.1, Waters Corporation) and protein spectra were deconvoluted by Waters MaxEnt1 algorithm. Myoglobin was used as reference for spectra calibration.

2.14 Tryptic digest – ESI orbitrap

Enzymatic in-gel digestions of Qβ conjugates were performed following a standard protocol[46]. Follow-up analysis was carried out on an Orbitrap Fusion (Thermo Scientific) connected to a Dionex Ultimate 3000 NCS-3500RS Nano LC system. Each sample was loaded for 5 min at a flow rate of 5.6 µL/min (2% acetonitrile, 0.05% trifluoroacetic acid) onto an Acclaim PepMap 100 C_{18} (3 µm, 75 µm × 20 mm) pre-column, followed by gradient elution (10% acetonitrile, 0.1% formic acid for 7.8 min, 18% acetonitrile in 1 min, followed by 30% acetonitrile in 20 min and 50% acetonitrile for another 5 min, then 80% acetonitrile in 4 min, flow = 200 nl/min) on a PikoTip column (75 µm × 250 mm) equipped with ReproSil-Pur 120 C_{18}-AQ 3 µm material. Mass spectra were obtained in a range of 350–1500 m/z with a resolution of 12000. Subsequent MS/MS data were obtained by electron-transfer dissociation to detect intact carbohydrate modifications.

2.15 Bioconjugation

Conjugation reactions were performed following a published protocol[25]. In the following, a typical conjugation procedure is described. To 500 µL of a 1.2 µM Qβ[Hpg] capsid solution (213.5 µM coat protein ≙ Hpg concentration) were added 90 eq. of the respective azido sugar, dissolved in 250 µL of 100 mM potassium phosphate buffer. Stock solutions of CuBr (99.999% trace metal basis, 10 mg/mL) and TEOTA (100 mg/mL) in acetonitrile were prepared. Subsequently, 187.6 µL of the CuBr solution and 72.6 µL of the TEOTA solution were mixed and 200 µL of the resulting Cu/ligand mix were transferred to the protein/sugar mixture. Reaction proceeded at 25°C at 800 rpm on a thermoshaker for 30 min. Another 100 µL portion of the Cu/ligand mix were added to the reaction and after additional 1.5 h the precipitate was removed by centrifugation and large excess of low molecular weight compounds was reduced by spin filtration. Purification of the reaction crude was again achieved by sucrose gradient ultracentrifugation (125,000 x g, 4.5 h, 4°C in a SW40 Ti rotor, 10-40% gradient). The relevant fractions were identified by SDS-PAGE, pooled, concentrated and washed in 30 kDa cut-off centrifugal filter units. Further polishing steps included dialysis against EDTA-containing potassium phosphate buffer (5 mM EDTA) and SEC on an Äkta FPLC system equipped with a Superose6 column.

The synthesized conjugates were characterized by intact protein ESI-MS to confirm successful conjugation and determine With our experimental set up, we cannot completely rule out the presence of Met traces in samples.[47] This incorporation originates from Met metabolic turnover in bacterial hosts as well as partial presence at the N-terminus due to incomplete cleavage by aminopeptidases as reported in other systems.[48] If the N-terminal Met was replaced by Hpg a second conjugation can occur, which we observed as minor side product in MS spectra. Tryptic digest followed by LC-MS/MS analysis was used to confirm

the correct position of the modification. Residual copper content after copper-catalyzed bioconjugation reaction was determined exemplary for **Qβ[HPG]** and **Qβ[Sia1]** by ICP-MS measurements (Table S 1). The copper content was increased more than 20-fold after the reaction (Entry 1 vs. Entry 2), if no dialysis against EDTA buffer was performed. After dialysis, copper levels were reduced to initial levels and below (Entry 3, three samples measured).

Table S 1: ICP-MS measurements of the copper content in Qβ samples before CuAAC, after CuAAC without dialysis and after CuAAC with dialysis as purification step.

Entry	Sample	Copper content in a 100 nM capsid sample
1	**Qβ[HPG]**	0.7 µM
2	**Qβ[Sia1]** no dialysis	15.5 µM
3	**Qβ[Sia1]** dialysis	< 0.5 µM

2.16 Cryo-electron microscopy

For binding experiments 15 µl of Qβ phage capsids (concentration 200 nmol/L) were incubated with 15 µL of influenza virus A/X 31 (~1 mg/mL total protein) with gentle agitation for 30 min at room temperature. Perforated (1 µm hole diameter) carbon film-covered microscopical 200 mesh grids (R1/4 batch of Quantifoil, MicroTools GmbH, Jena, Germany) were hydrophilized by 60 s glow discharging at 8 W in a BALTEC MED 020 device (Leica Microsystems, Wetzlar, Germany). Then 5 µL of the corresponding sample were pipetted to the hydrophilized grid and the supernatant fluid was immediately removed with a piece of filter paper until an ultrathin layer of the sample solution (typical thickness of 100-250 nm) was obtained spanning the holes of the carbon film. The sample was instantly vitrified by plunging the grids into liquid ethane using a guillotine-like apparatus. The vitrified sample was subsequently transferred under liquid nitrogen into a Tecnai F20 TEM (ThermoFisher Scientific Inc., Waltham (MA), USA) equipped with a field emission gun operating at 160 kV by the use of a Gatan tomography cryo-holder (Model 914). Microscopy was carried out at a 94 K sample temperature using the low-dose protocol of the microscope. Micrographs were taken with a FEI Eagle 4k × 4k CCD camera using the twofold binning mode. To generate stereo images, the same image section was recorded at two different tilt angles (4° and -4°) using the Compustage of the microscope. The resulting micrographs were aligned using the software StereoPhoto Maker (Masuji Suto, Japan).

2.17 Cryo-electron tomography

Tomograms were acquired on a Titan Krios™ transmission electron microscope (ThermoFisher Scientific Inc., Waltham (MA), USA) operating at 200 kV and equipped with a Volta phase plate. Single axis tilt series (±64° in 2° tilt angle increments) were recorded with a Falcon-II 4k × 4k direct electron detector at full resolution (29 K primary magnification) with a total dose less than 70 $e^-/Å^2$. Tomogram reconstruction was done using ThermoFisher Inspect3D software. Manual segmentation and 3D rendering were performed using Amira, Version 6.0 (FEI, Oregon, USA).

3 Biophysical and biological methods

3.1 Cell culture

The cell lines MDCK-II (Madin-Darby canine kidney epithelial) (ATCC, Germany), and A549 (*Human* lung *adenocarcinoma* epithelial) (CLS, Germany) were maintained in DMEM (supplemented with 10% fetal calf serum (FCS), 2 mM L-glutamine, 100 U/ml penicillin and 100 µg/ml streptomycin at 37 °C and 5% CO_2.

3.2 Influenza virus strains

Influenza A/X31 virus (H3N2; HA and NA genes derived from A/Aichi/2/68, reassorted with internal segments of A/Puerto Rico/8/1934 (H1N1)), A/mallard/Germany/439/2004 (H3N2), A/Puerto Rico/8/1934 (H1N1), A/WSN/1933 (H1N1) or A/Teal/Germany/2005 (H5N1; HA and NA genes derived from A/Teal/Germany/2005, reasserted with internal segments of A/WSN/1933 (H1N1), kindly provided by Dr. Mair, Molecular Biophysics, HU Berlin) were harvested from allantoic fluid of embryonated chicken eggs. A/Panama/2007/1999 (H3N2) was propagated in MDCK-II cells, and the Influenza B/Thüringen/2/2006 patient isolate was propagated on Vero E6 cells. Harvested stock virus was clarified upon low speed centrifugation (300 x g, 10 min) and stored as aliquots at -80 °C. Viral titers were assessed by standard plaque assay titrations on MDCK-II cells.

3.3 Microscale thermophoresis

Measurements were performed using a Monolith NT.115 instrument (Nanotemper), and standard glass capillaries (Nanotemper) at 22 °C. Each inhibitor was twofold serially diluted and mixed with equal amounts of R18 labeled X31 (4 HAU, c_{final}≈0.1 nM virus particles). After a short incubation, the inhibitor-virus mix was loaded in glass capillaries and measured for initial fluorescence and change in fluorescence upon a thermophoresis measurement (MST power: 80%, green LED power 100%). For analysis, the T-jump with 5 s thermophoresis was used and gated as shown in the supplementary analytical data. In order to determine the noise level, triplicates of the same virus dilution were measured leading to ΔF_{virus}≈ 6 FU. The change in fluorescence was expressed as fraction bound of the maximum fluorescence in the bound state. Apparent dissociation constants were deduced from a binding saturation fit of mean values of independent experiments. The function for fitting is derived from the law of mass action.

$$F = \frac{1}{2B}\left(B + L + Kd_{app} - \sqrt[2]{\left(B + L + Kd_{app}\right)^2 - 4B * L}\right)$$

with L being the ligand concentration at each data point, B being the constant concentration of the fluorescent molecule, F being the fraction of the complex between B and L to the total amount of binding sites (B) at each data point.

3.4 Hemagglutination inhibition assay

Different virus strains were incubated with human or chicken erythrocytes, respectively, to yield agglutination (in the absence of an inhibitor) and concentration-dependent inhibition of agglutination (in the presence of an inhibitor). Inhibitors were twofold serially diluted in Dulbecco's phosphate buffered saline (DPBS). Then, four hemagglutination units (HAU) containing $4 \cdot 10^7$ virus particles were added to all wells. Viral particle concentration was estimated as described by Desselberger et al.[49]. After 30 min incubation at room temperature (rt), 50 µl of a 1% erythrocyte solution (~$2 \cdot 10^6$ cells μl^{-1}) was added, gently mixed and incubated for 60 min at rt. For human pathogenic strains human erythrocytes (α-2,6'-sialosugars), for avian pathogenic strains chicken erythrocytes (α-2,3'-sialosugars) were

used. The inhibitor constant K_i(HAI) reflects the lowest inhibitor concentration, which is necessary to achieve complete inhibition of hemagglutination caused by the influenza virus. To check for full hemagglutination inhibition, the microtiter plate was tilted by 60° to cause droplet formation from the red blood cell pellet[50].

3.5 Cytotoxicity and cytopathic effect inhibition assay

Viral infection inhibition and cytotoxicity were monitored using a Cell Titer Glo (Promega) assay according to the standard protocol of the manufacturer. The provided reagents detect the overall ATP level of cells via luciferase. The ATP level being proportional to the number of viable cells was recorded upon luminescence detection with a plate reader (Spark, Tecan). Cells infected with Influenza A virus cause a cytopathic effect, which goes along with reduced number of cells or cell viability, respectively.

Here, 4,000 A549 cells were seeded one day before infection in a white 384 well plate. On the next day, A/X31 was pretreated with Qβ phages in a twofold dilution series for 30 min at rt under slight agitation. Then, the inhibitor-virus (MOI 0.05) mix was transferred to cells, following incubation for 24 h at 37 °C. Cytotoxicity was assessed adding inhibitor without virus to cells. Following, 25 µl Cell Titer Glo solution was added to each well and incubated for 10 min at rt. Finally, luminescence was measured, and data were normalized to maximum viral cytopathogenicity as follows:

$$Cell\ viability\ (\%) = \frac{(Infected_{treated} - Infected_{untreated})}{(Uninfected_{untreated} - Infected_{untreated})}$$

Dose response curves of mean values (n≥3) were fitted using a four parametric logistic fit to obtain IC_{50} values. The asymmetric standard error (SE) of the fit is given as $\log IC_{50}$.

3.6 Infection inhibition assay

A/Panama/2007/1999 (H3N2) virus was pretreated in an inhibitor titration experiment with Qβ[Sia1] and maintained for 30 min at rt. The day before, $5x10^4$ A549 cells were seeded in an 8-well plate (ibidi). On the following day, the cells were washed once with $DPBS^{++}$ and infected with inhibitor or DPBS treated A/X31 (MOI 1) for 1 h on ice to synchronize the infection. Unbound virus was removed by aspiration of the supernatant, and subsequent washing with infection media (DMEM, 1% FCS). Following that, cells were incubated for 6 h at 37°C and analyzed for viral nucleoprotein expression by immunostaining as follows:

Cells were washed, fixed with 4% paraformaldehyde and permeabilized with 0.5% (w/v) triton X-100. Furthermore, the cells were blocked with blocking buffer ($DPBS^{++}$, supplemented with 3% BSA and 100 mM L-glycine) for 2 h at rt. Immunostaining was performed with a FITC-coupled mouse α-NP monoclonal antibody (preference for nuclear NP, Millipore, 1:500 in $DPBS^{++}$ with 1 % BSA), and a primary unlabeled mouse α-NP monoclonal (Millipore, 1:500 in $DPBS^{++}$ with 1 % BSA). The unlabeled antibody was detected using an Alexa488 labeled secondary goat α-mouse polyclonal antibody (preference for cytoplasmic NP; ThermoFisher Scientific; 1:1000 in $DPBS^{++}$ with 1 % BSA). Cellular DNA was stained using DAPI. Confocal microscopy was assessed using an Olympus FV 1000 microscope. Acquired images were analyzed for viral NP expression using an ImageJ software as follows: Cells were automatically identified by an ImageJ script from the DAPI signal of the stained nuclei. Each object, representing one cell, was further analyzed for the fluorescence intensity coming from the FITC coupled α-NP monoclonal antibody. Median fluorescence intensities of all detected objects (n>1000) were expressed in ratio to the

infected, DPBS-treated cells. Statistics were performed using a one-way ANOVA analysis with a Dunnett's multiple comparison test to the infected, DPBS treated control.

3.7 Inhibition of viral propagation in cell culture

MDCK-II cells were infected with IAV A/X31 or A/Panama/2007/1999 with a MOI of 0.01 for 45 min. Unbound virus was washed off, followed by incubation in infection medium (MEM supplemented with 1mM glutamine, 0.2 % bovine serum albumin, 1 mg/ml TPCK-trypsin and 1% penicillin/streptomycin) containing different concentrations of Qβ capsid [Sia1]. After 24 h virus titers in the supernatant were determined by plaque titration on MDCK-II cells. Results are given as plaque forming units per ml (PFU/ml). Values were log-transformed and normalized for IC_{50} calculation with GraphPad Prism 7.

3.8 *In vivo* infection inhibition study

Animals were maintained and handled according to the Directive 86/609/EEC of the European Community Council and to the institutional, state and federal guidelines. All animal protocols were approved by the ethics committee of the Landesamt für Gesundheit und Soziales (LAGeSo, Berlin, Germany) with registration number G0011-15. Animals were housed under standard conditions of 12 h light/dark cycle and given access to food and water *ad libitum*. Experiments were performed with 8 weeks old BALB/c mice (Charles River) as previously described[51]. First, mice were sedated by an intraperitoneal injection of 200 µl Cepetor (4 µg/100 µl) and anesthetized by isofluran inhalation. Then, A/X31 virus was preincubated with inhibitor for 30 minutes at rt in $DPBS^{++}$ before the 25 µl virus-inhibitor mix was distributed to both nostrils of the mice. After complete uptake of the virus-inhibitor solution, mice were revitalized, by injecting 200 µl antisedan (2 µg/100 µl) intraperitoneally. Groups of five mice were maintained per cage and experiment for 10 days. The mice were weighed daily and the influenza virus infection related loss in body weight was expressed as percentage of the initial body weight. As soon as animals reached a maximum score of 3 for signs of discomfort and suffering or if a loss in body weight of more than 20 % was observed, according to the regulations, mice were sacrificed upon cervical dislocation. At the end of the experiment (day 10), all mice were sacrificed upon cervical dislocation.
Data were statistically analyzed by comparison of infected, inhibitor treated mice to infected, DPBS treated animals, conducting a one-way ANOVA and Dunnett's multiple comparison test.

3.9 *Ex vivo* infection of human lung tissue

Tumor-free normal human lung tissue was cut into small pieces (weight approx. 0.1 – 0.2 mg per piece) and incubated in RPMI 1640 medium overnight to wash off clinically applied antibiotics. The study was approved by the ethics committee at the Charité clinic (projects EA2/050/08 and EA2/023/07) and written informed consent was obtained from all patients. The infection experiments were done in RPMI 1640 infection medium (supplemented with 0.3 % bovine serum albumin and 2 mM L-glutamine) at 37 °C with 5 % CO_2 as described previously[52-54]. For replication analyses, human lung tissue explants were inoculated with 2×10^5 PFU in RPMI 1640 medium for 1.5 h at room temperature. Excess virus was removed by washing with phosphate-buffered saline (DPBS) and lung tissue was incubated for 48 hpi (hours post infection) in RPMI infection medium containing 10 nM of Qβ[Sia1] inhibitor. At 24 hpi, an additional 10 nM of Qβ[Sia1] inhibitor was added to the corresponding well to test if the inhibitory effect can be boosted ("10 + 10 nM"). For the experiment, tumor-free

tissue specimens from four donors. For replication analysis, at 0, 16, 24 and 48 hpi supernatants of infected lung tissue were harvested and viral titers were determined by standard plaque titration assay.

3.10 Analysis of proinflammatory and antiviral cytokines

The immunogenicity of Qβ phage capsids was studied in comparison to capsids which underwent additional purification to remove residual LPS. Here, an aqueous two-phase separation (ATPS) protocol was adapted from Branston and colleagues[55], and conducted as follows: To a 500 nM capsid solution in 100 mM KPi-buffer, pH = 7.4, 1 % (v/v) Triton X-114 was added at 4 °C, mixed and incubated for 5 min at 4 °C. In the meantime, Bio-Beads SM-2 (Bio-Rad) were soaked in KPi buffer for 5 min. The sample was warmed to 37 °C, incubated at this temperature for another 5 min and centrifuged at 37 °C for 1 min at 15.000 x g. The soaking buffer from the BioBeads was mostly discarded and the upper, detergent-poor fraction from the sample was transferred to the Bio-Bead suspension. Following, 2 h incubation at rt with gentle inversion the Bio-Beads were removed upon filtration through a 0.45 µm syringe filter. Aliquots for determination of endotoxin content were subsequently frozen at -80 °C until the day of the experiment.

Endotoxin concentration was determined by rFC-assay (PyroGene™ Recombinant Factor C Endotoxin Detection Assay, Lonza). Samples were diluted 1:100 in endotoxin-free water for the assay. The diluted samples showed responses at the assay's lower detection limit, corresponding to endotoxin concentrations of < 1 EU/mL in the non-diluted samples (n = 4). The spike recovery under the employed assay conditions was 86±15%, n = 4. (Spike recovery is a parameter for validity of results, allowed range is 50-200%).

Cytokine release was measured from supernatants 48 h after lung tissue treatment using ELISA Ready-SET-Go! kits (ThermoFisher) for TNF-α and IL-1β, and a human IFN-β ELISA Kit from PBL Assay Science. Measurements were conducted according to the protocols of the manufacturers.

4 Supplementary Notes

Sia duplets and triplets:

A Qβ capsid has a diameter of approximately 25 nm. It consists of 90 protein dimers that form a truncated icosahedron. Therefore, the anchoring points of the Sia units are placed along the edges of hexagonal or pentagonal substructures (**Supplementary Figure 2a**). Thereby, two thirds of all edges connect a hexagon-hexagon substructure and one third connect hexagon-pentagon substructures.

The distance between neighboring Sia units depends on whether these units are found along the edge of a hexagonal or pentagonal substructure. In **Supplementary Figure 2b** Sia triplets within neighboring hexagonal-pentagonal substructures are shown, whereas **Supplementary Figure 2c** shows Sia triplets within two neighboring hexagonal substructures. Similarly, **Supplementary Figure 2d-f** shows Sia duplets within neighboring hexagonal-pentagonal substructures (**Supplementary Figure 2d** and **e**) or two neighboring hexagonal substructures (**Supplementary Figure 2f**).

The distance between Sia duplets (indicated by dashed lines in **Supplementary Figure 2d-f**) varies between 3.2 nm and 7.2 nm, whereas Sia triplets (**Supplementary Figure 2b** and **c**) exhibit an edge length of d_1=5.0 nm (dashed line), d_2=5.9 nm (solid line) or d_3=6.2 nm (dotted line).

As we will show further below, the binding of the Qβ capsid towards HA is dominated by the two smallest Sia triplets.

Dissociation constant:

The dissociation constant K_d is defined as

$$K_\mathrm{d} = \frac{[L][R]}{[LR]}, \qquad (1)$$

with [L] the concentration of free ligands, i.e. the concentration of unbound Qβ capsid, [R] the concentration of free receptors, here the HA-trimers, and [LR] the concentration of bound ligand-receptor pairs. For dilute concentrations interaction between ligands as well as interactions between receptors can be neglected and the dissociation constant follows from the ideal gas approximation:

$$K_\mathrm{d} = \frac{q_\mathrm{L}/V\, q_\mathrm{R}/V}{q_\mathrm{LR}/V}, \qquad (2)$$

with q_X the partition function of species X and V the volume of the system.

In the following we derive the partition function of free and bound ligands and receptors, from which we deduce an expression for the dissociation constant.

The partition function of the free ligand reads:

$$q_\mathrm{L} = V 8\pi^2 q_{\mathrm{Q}\beta} \prod_{j=1}^{180} q_\mathrm{Sia} \Omega_\mathrm{Sia} \int_V d\mathbf{r}_j P_\mathrm{str}(\mathbf{r}_j, n), \qquad (3)$$

with V the volume of the entire system, $8\pi^2$ accounts for the angular space of a rigid body, which is the product of the area of a unit sphere 4π, times a factor 2π for rotations around the body axis. The partition function over the internal degrees of freedom of the Qβ capsid is denoted as $q_{\mathrm{Q}\beta}$, while the partition function over the internal degrees of freedom of a single Sia unit is denoted as q_Sia. In **Eq.3** we multiply the contribution from all 180 Sia units, and

their EG linkers. The probability to stretch the j-th EG linker, consisting of n monomers, along the end-to-end vector $\mathbf{r}_\mathrm{j}$ is described by $P_\mathrm{str}(\mathbf{r}_\mathrm{j}, n)$. We determined P_str from molecular dynamics simulation, as described in detail further below. The angular space of the Sia unit is denoted as Ω_Sia. Steric repulsions between Sia and the linker significantly restrict the degrees of freedom of Sia (schematically indicated in Fehler! Verweisquelle konnte nicht gefunden werden.Fehler! Verweisquelle konnte nicht gefunden werden.**Supplementary Figure 2g**). Hence, the angular space of each Sia unit is smaller than the angular space of a free rigid body ($8\pi^2$). To quantify the restriction of angular degrees of freedom, we define the angular restriction factor $\omega_\mathrm{Sia} = \Omega_\mathrm{Sia}/8\pi^2$. From a fit to the experimental data (**Fig. 3c** in the main text) we determine a value of ω_Sia=0.05. For comparison, in the limiting case without any steric exclusion, the angles ϕ and ψ are limited by 2π, whereas θ is limited by π, which leads to ω_{Sia}=1.0. In a previous study an angular restriction factor of ω_{sia}=0.03 was found for inhibitors against the pentavalent cholera toxin and the heptavalent anthrax receptor[56]. The slightly larger value of ω_{Sia}=0.05 that we obtained for the Qβ capsid in the present work might arise due to the different linker and ligand chemistries as well as due to the fact that the angular restriction factor also accounts for interactions between the linker and the HA surface.

To simplify the partition function q_L of the free ligand (**Eq.3**) we impose that the stretching probability is normalized by $\int_V d\mathbf{r}_j P_{str}(\mathbf{r}_j, n) = 1$. Hence, q_L becomes:

$$q_\mathrm{L} = V 8\pi^2 q_{\mathrm{Q}\beta} (q_\mathrm{Sia}\Omega_\mathrm{Sia})^{180} \qquad (4)$$

For free monovalent Sia the partition function of the Qβ capsid as well as the restricted angular space Ω_Sia in **Eq.4** are omitted and the partition function reads:

$$q_\mathrm{L}^\mathrm{mono} = V 8\pi^2 q_\mathrm{Sia} \qquad (5)$$

The partition function of a bound ligand receptor pair includes three binding modes:

$$q_\mathrm{LR} = \sum_{i=1}^{3} q_\mathrm{LR}^{(i)} \qquad (6)$$

in which the i-th binding mode represents $i = 1,2,3$ bound Sia units.

The partition function of the i-th binding mode factorizes into the contribution from the receptor q_R and contributions from the bound ligand:

$$q_\mathrm{LR}^{(i)} = q_\mathrm{R} N(i) q_{\mathrm{Q}\beta} \int d\mathbf{r}_{\mathrm{Q}\beta} \int d\boldsymbol{\omega}_{\mathrm{Q}\beta} \prod_{j=1}^{180} q_\mathrm{Sia}\Omega_\mathrm{Sia} \int_V d\mathbf{r}_j P_\mathrm{str}(\mathbf{r}_j, n) \qquad (7)$$
$$\times \left[\frac{2}{3} \sum_{\{N_{6,6}\}} \sum_{\{k\}} \prod_{k=1}^{i} q_\mathrm{Sia}\Omega_\mathrm{bp} V_\mathrm{bp} e^{-\beta\Delta G} P_\mathrm{str}(\mathbf{r}_k, n) + \frac{1}{3} \sum_{\{N_{5,6}\}} \sum_{\{k\}} \prod_{k=1}^{i} q_\mathrm{Sia}\Omega_\mathrm{bp} V_\mathrm{bp} e^{-\beta\Delta G} P_\mathrm{str}(\mathbf{r}_k, n) \right]$$

$N(i)$ in **Eq.7** is a permutation factor, with $N(i)$=180/i. In case of monovalent binding $N(1) = 180$, which reflects the number of Sia units and hence the number of binding permutations per capsid. For divalent binding of a certain Sia duplet, there are 90 equivalent Sia duplets ($N(2) = 90$). All equivalent Sia duplets are obtained by rotation around the capsid axes. Similarly, considering the capsid structure and rotating a certain Sia triplet around the capsid axes, leads to 60 equivalent Sia triplets, hence $N(3) = 60$.

As was discussed in detail in the previous section, the Qβ capsid forms hexagonal and pentagonal substructures. $\sum_{\{N_{6,6}\}}$ and $\sum_{\{N_{5,6}\}}$ denote the sums over all monomers, duplets (indicated as dashed lines in **Supplementary Figure 2d-f)** or triplets (indicated as red triangles in **Supplementary Figure 2b,c)** within two neighboring hexagonal or a hexagonal

and a pentagonal substructure. The prefactors 2/3 and 1/3 account for the ratio of hexagonal and pentagonal substructures. $\sum_{\{k\}}$ is the sum over all permutations by which i Sia units can bind to the three receptor binding pockets for a given capsid position and capsid orientation. Different permutations between the three HA binding pockets and the i Sia units result in different linker stretching and hence influence P_{str}.

The position and orientation of the Qβ capsid relative to the receptor is denoted as $\mathbf{r}_{\mathrm{Q}\beta}$ and $\boldsymbol{\omega}_{\mathrm{Q}\beta}$ (schematically shown in **Supplementary Figure 2h**), where $\boldsymbol{\omega}_{\mathrm{Q}\beta} = (\phi, \theta, \psi)$ summarizes the Euler angles by which the capsid can rotate. The volume of the receptor binding pockets and the angular space of Sia inside the binding pockets are described by V_{bp} and Ω_{bp}, respectively. Each bound Sia gains the binding free energy ΔG, whereby β denotes the inverse thermal energy.

For a bound monovalent Sia unit, we omit all terms in **Eq.7** associated with the linkers and the capsid. Hence, q_{LR} simplifies to:

$$q_{\mathrm{LR}}^{\mathrm{mono}} = q_{\mathrm{R}} q_{\mathrm{Sia}} \Omega_{\mathrm{bp}} V_{\mathrm{bp}} e^{-\beta \Delta G} \qquad (8)$$

Based on **Eq.2**, **5** and **8** we write the dissociation constant of a monovalent Sia as:

$$K_{\mathrm{mono}} = \frac{8\pi^2}{\Omega_{bp}} \frac{e^{\beta \Delta G}}{V_{\mathrm{bp}}} \qquad (9)$$

Combining **Eq.2**, **4**, **6** and **7** we can now derive an expression for the dissociation constant of the entire multivalent Qβ capsid.

$$K_{\mathrm{d}} = \left[\sum_{i=1}^{3} \frac{\int d\mathbf{r}_{\mathrm{Q}\beta} \int d\omega_{\mathrm{Q}\beta} N(i) \left[\frac{2}{3} \sum_{|N_{6,6}|} \sum_{\{k\}} \prod_{k=1}^{i} P_{\mathrm{str}}(\mathbf{r}_k, n) + \frac{1}{3} \sum_{|N_{5,6}|} \sum_{\{k\}} \prod_{k=1}^{i} P_{\mathrm{str}}(\mathbf{r}_k, n) \right]}{K_{\mathrm{mono}}^{i} \omega_{\mathrm{Sia}}^{i}} \right]^{-1} \qquad (10)$$

We evaluate the integrals over $\mathbf{r}_{\mathrm{Q}\beta}$ and $\boldsymbol{\omega}_{\mathrm{Q}\beta}$ in **Eq.10** numerically by Monte Carlo integration. We thereby model the receptor as a planar surface on which the binding pockets form an equilateral triangle. Furthermore, we impose that the midpoint of the Qβ capsid, which we describe as a sphere with a diameter of 25 nm, cannot penetrate the receptor plane.

In **Supplementary Figure 2j** we show the inverse of the dissociation constant K_{D}^{-1} (**Eq. 10**), since it allows to disentangle the contributions from mono-, di- and trivalently bound Qβ capsids. The angular restriction factor is set to ω_{Sia}=0.05. The stretching probability P_{str} is obtained from molecular dynamics simulation (**Eq.13**). The contribution of all Sia duplets (green line) is summed up, while for Sia triplets (red lines) the contribution of each triplet (**Supplementary Figure 2d**) is shown individually. As we can see from **Supplementary Figure 2j** the binding behavior of the Qβ capsids is dominated by the two smallest Sia triplets. Both triplets occur in the hexagonal as well as pentagonal substructure of the capsid (**Supplementary Figure 2d**). To quantify the impact of trivalently bound capsids, we compare the dissociation constant taking all binding modes into account (inverse of the black line in **Supplementary Figure 2d**), denoted by K_{all} , and the dissociation constant considering only the contribution of the two smallest Sia triplets (inverse of the sum over the solid and dashed red lines in **Supplementary Figure 2j**), denoted by K_{tri}. We find that the ratio $\gamma = (K_{\mathrm{tri}} - K_{\mathrm{all}})/K_{\mathrm{all}}$ varies between $\gamma = 4 \cdot 10^{-6}$ for n=1 and $\gamma = 0.15$ for n=10. Hence, the dissociation constants differ by less than 15%, even for the longest EG linkers.

The dissociation constant (**Eq.10**) is therefore well approximated by:

$$K_{\mathrm{d}} = \frac{K_{\mathrm{mono}}^3 \omega_{\mathrm{Sia}}^3}{60(C_3(d_1{=}5.0nm)+C_3(d_2{=}5.9nm))}, \qquad (11)$$

where the factor 60 in the denominator accounts for the fact that we find 60 Sia triplets with an edge length of d_1=5.0 nm and 60 Sia triplets with an edge length of d_2=5.9 nm on the capsid surface. The integral over the capsid position and orientation leads to the cooperativity factor C_3, with

$$C_3 = \int d\mathbf{r}_{\mathrm{Q}\beta} d\boldsymbol{\omega}_{\mathrm{Q}\beta} \sum_{\{k\}} \prod_{k=1}^{3} P_{\mathrm{str}}(\mathbf{r}_k, n)\ . \qquad (12)$$

Comparison of different virus strains:

To compare the distance between neighboring binding pockets, for various virus strains, we calculate the distance between the C2 atoms of the Sia unit of a H1-(pdb: 1rvz), H3-(pdb-entry: 1hgg) and a H5-(pdb: 5e2z) hemagglutinin. We find that within these three structures, the distance between the binding pockets varies by less than 2Å. With regard to the vertical position of the binding pockets, we find that in all three structures residue 159 (159Gly for 1rvz, 159Ser for 1hgg, 159Asn for 5e2z) exhibits the largest vertical distance, with respect to the Cα-position, from the plane spanned by the Sia units. The vertical distance between residue 159 and the Sia units varies between 1.2nm for the H3-structure and 1.5nm for the H5-structure. Hence, the variation for the binding pocket position, in the range of 2-3Å, is smilingly small, but in the same range as the average linker length fluctuations of short EG linkers with less than five units (**Supplementary Figure 2o**). The combination of slight variations in the binding pocket position and the limited fluctuation range of short EG linkers, might explain, why virus strains including H3 receptors show optimal inhibition for Qβ[Sia1], while virus strains including H1 receptors exhibit optimal inhibition for Qβ[Sia3] and Qβ[Sia5]. Another parameter that slightly varies between different virus strains is the monovalent dissociation constant K_{mono}. The impact of K_{mono} on the dissociation constant K_{d} is shown in **Supplementary Figure 2i.** A slight increase of K_{mono} by a factor of 1.5 causes the dissociation constant K_{d} to exceed values of 100nM for EG linkers with more than two EG units.

Steric shielding:

In the following we describe a simple estimate for the number of Qβ capsids necessary to inhibit an entire virus. Due to its size and spherical shape, a Qβ capsid can effectively shield an area on the virus surface that is much larger than the area of direct contact. Describing the Qβ capsid as a sphere with radius R_{c} = 12.5 nm and the virus as a sphere with radius R_{v} = 50 nm the minimal and maximal number of Qβ capsids necessary to cover the entire virus read[57]:

$$N_{min} = \frac{R_{\mathrm{v}}}{R_c} + 2 \qquad (13)$$

$$N_{max} = \frac{1}{1-\sqrt{(R_v/R_c)(2+R_v/R_c)/(1+R_v/R_c)^2}} + 1 \qquad (14)$$

According to (**Eq.13**) and (**Eq.14**) the number of Qβ capsids per virus varies between N_{min}= 6 and N_{max} = 50. The minimal number N_{min} refers to a capsid arrangement with a maximal separation between the capsids that still inhibits the attachment of the virus to a planar surface (**Supplementary Figure 2k**). The maximal number N_{max} corresponds to a random closed packing of capsids on the virus surface (**Supplementary Figure 2k**).

Number of HA spikes interacting with a single Qβ capsid:

To quantify the interaction between a capsid and the virus, the contact area between the two binding partners has to be estimated. If the virus is flexible enough to wrap around the capsid, several HA trimers can participate in the binding process. In contrast, if the virus remains in a spherical shape, the interaction is limited to a single HA trimer.

In **Supplementary Figure 2k** the deformation of a virus, bound to a spherical capsid, is depicted schematically. The larger the indentation depth d, the larger becomes the deformation energy as well as the contact area A_c. Whereby, the contact area is given by $A_\mathrm{c} = 2\pi R_\mathrm{c} d$, with R_c the radius of the capsid. Based on AFM-measurements Li et al.[58] determined a linear relation between deformation force and indentation depth d, with a force constant of k=27.4 pN/nm for a virus of diameter 100 nm. The free energy F of the deformed virus can be estimated as:

$$F = -gA_\mathrm{c} + \frac{k}{2}d^2 \qquad (15)$$

The first term accounts for the binding energy, with g the binding energy per area and the second term describes the elastic deformation.

We assume an average distance between neighboring HA-trimers[58] of D_HA = 10 nm and a binding energy[60] per HA-binding pocket of $\Delta G = 20 k_\mathrm{B} T$. If all three binding pockets are occupied, an upper limit for a binding energy per area is obtained as:

$$g = \frac{3\Delta G}{\pi (D_\mathrm{HA}/2)^2} \qquad (16)$$

Minimizing the free energy with respect to d leads to an indentation depth of:

$$d = \frac{6\Delta G R_\mathrm{c}}{(D_\mathrm{HA}/2)^2 k} \qquad (17)$$

With a capsid radius R_c = 12.5 nm an indentation depth $d \approx 2.2$ nm is obtained, or equivalently a contact area of A_c = 172 nm^2. For comparison, the area per HA-trimer is estimated by $\pi(D_\mathrm{HA})^2$ = 157 nm^2. Comparing the contact area and the area per HA-trimer, we conclude that the interaction between virus and capsid is limited to single HA-trimers.

Angular restriction factor - MD simulation:

Based on the experimental data (**Figure 3c** in the main text) we fit **Eq. 11** with an angular restriction factor of ω_{sia}=0.05. To verify that this value is determined by the angular space available to the Sia unit, we perform molecular dynamics (MD) simulations of a single Sia unit connected to a -CH_2-CH_2-O-CH_3 linker. The Euler angles φ, θ, ψ that describe the orientation of the Sia unit relative to the linker are shown schematically in **Supplementary Figure 2m**. Scatterplots of the $\varphi - \psi$, $\varphi - \theta$ and $\psi - \theta$ angles obtained over a simulation time of 200ns are shown in **Supplementary Figure 2n**.

The angular restriction factor is defined by the integral

$$\omega_{sia} = \frac{1}{8\pi^2} \int_0^{2\pi} \int_0^{2\pi} \int_0^{\pi} \sin(\theta)\, \mathrm{d}\theta\, \mathrm{d}\varphi\, \mathrm{d}\psi \qquad (14)$$

As we can see from **Supplementary Figure 2n**, θ is always restricted to values 54°< θ<70° (indicated as dashed lines in **Supplementary Figure 2n**) independent of the φ and ψ. Hence, the angular restriction factor factorizes into

$$\omega_{sia} = 0.0031 \int_0^{2\pi} \int_0^{2\pi} \mathrm{d}\varphi \, \mathrm{d}\psi \qquad (15)$$

To determine the integral over φ and ψ numerically, each axis in the φ-ψ-scatterplot is divided into 70 equally distant bins, dividing the φ-ψ-plane into 4900 equally sized grid fields. The sum over the area of all grid fields containing at least one data point is equivalent to the integral over φ and ψ. Based on the scatterplot in **Supplementary Figure 2n**, we obtain a value of ω_{sia}=0.041, which is in good agreement with the fitted value of ω_{sia}=0.05. The difference between the fitted and the simulated value might arise due to a slightly repulsive interaction between the linker and the receptor in the range of $\ln(0.05/0.041)k_BT$=0.2 k_BT per linker.

EG linker - MD simulation:

The Sia units are connected to the capsid via EG linkers. The EG length and extensibility significantly influences the binding behavior. We perform molecular dynamic simulation of short EG oligomers (CH_3-O-[CH_2-CH_2-O-]$_n$-CH_3, with $n \in [1,10]$) in water and determine the probability distribution $P_{\mathrm{str}}(r_{ete})$ of the end-to-end distance r_{ete}. The end-to-end distance is measured between the outermost oxygen atoms. In **Supplementary Figure 2o** the stretching probability $P_{\mathrm{str}}(r_{ete})$ is shown for all EG oligomers. The stretching probability is normalized by the condition: $4\pi \int dr_{\mathrm{ete}} r_{\mathrm{ete}}^2 P_{\mathrm{str}}(r_{\mathrm{ete}})$=1. P_{str} is fitted by a normal distribution:

$$P_{\mathrm{str}}(r_{\mathrm{ete}}) = \frac{1}{2(2\pi)^{3/2}(\mu^2+\sigma^2)\sigma} \exp\left[-\frac{(r_{\mathrm{ete}}-\mu)^2}{2\sigma^2}\right] \qquad (16)$$

The fit parameters μ and σ are indicated in the legend of **Supplementary Figure 2o**.

Molecular dynamics (MD) simulations

The MD simulations of EG oligomers in water are performed with the GROMACS simulation package[61] version 4.6.8. The following simulation parameters are used: The time step is set to 2 fs. The temperature is set to 300 K. For temperature-/pressure coupling the v-rescale[62]/Parrinello-Rahman[63] algorithm with a relaxation time of 0.1 ps/0.5 ps is chosen. The pressure is set isotropically to 1 bar with a water compressibility of $4.5 \cdot 10^{-5}$bar^{-1}. All simulations are performed with periodic boundary conditions in all three directions. The cut-off of non-bonded interactions is set to 1.0 nm. Long range electrostatic interactions are treated with the PME[64,65] method. The length of all covalently bound hydrogen bonds is fixed via a LINCS[66] algorithm, with a LINCS-order=4 and iteration number 1. The EG oligomers as well as the Sia unit connected to an EG-linker are solvated in tip3p water[67]. Cubic simulation boxes are used for all simulations. For the EG oligomers the initial edge size varies between 2.3nm and 6.2nm. For the Sia unit connected to an EG-linker the initial edge size is set to 3.5nm. To determine the end-to-end-distance distribution of individual EG oligomers the following simulation steps are performed: After an energy minimization a 200 ns NPT-simulation is performed. The first 10 ns are discarded in the analysis. To determine the angular restriction factor the following simulation steps are performed: After an energy minimization a 202ns NPT-simulation is performed. The first 2 ns are discarded in the analysis. The EG oligomers and EG linkers, respectively are parametrized with the charmm35r forcefield[68,69]. The Sia units are parametrized with the charmm carbohydrate forcefield[69]. The bonds, angles and dihedrals at the connection between Sia and the EG linker are parametrized as follows:

Bonds:

O_{sia}-C_{peg} → OCE-CCT2 (charmm35r)

Angles:

C_{sia} -O_{sia}-C_{peg} → CCT2-OCE-CCT2 (charmm35r)

O_{sia}-C_{peg}-H_{peg} → OCE-CCT2-HCT2 (charmm35r)

O_{sia}-C_{peg}-C_{peg} → OCE-CCT2-CCT2 (charmm35r)

Dihedrals:

C_{sia} - C_{sia} -O_{sia}-C_{peg} → CCT2- CCT2-OCE-CCT2 (charmm35r)

O_{sia} - C_{sia} -O_{sia}-C_{peg} → CCT2- CCT2-OCE-CCT2 (charmm35r)

C_{sia} -O_{sia}-C_{peg} -H_{peg} → CCT2-OCE-CCT2-HCT2 (charmm35r)

C_{sia} -O_{sia}-C_{peg} -C_{peg} → CCT2-OCE-CCT2-CCT2 (charmm35r)

O_{sia}-C_{peg} -C_{peg}-O_{peg} → OCE-CCT2-HCT2-OCE (charmm35r)

The atom names follow the nomenclature in reference 68.

Structure Optimization:

To superimpose the structure of the HA receptor and the Qβ capsid, we first align their crystal structures, such that the C2 atoms of the Sia units as well as the anchoring points of the EG linkers on the Qβ capsid (residue 16) lie in parallel planes. Subsequently the structures are rotated such that the triangles formed on the HA receptor as well as on the Qβ capsid are orientated in parallel. From a first structure optimization of one Sia unit connected to a linker with one EG unit, we obtain the optimal height separation between the HA receptor and the Qβ capsid. The second structure optimization includes all three Sia units, residue 16 from the Qβ capsid and the linker between them. The coordinates of the Sia units as well as residue 16 are taken from the crystal structure. Furthermore, the coordinates of the Sia units and residue 16 are fixed and only the positions of the linker atoms are left to optimize. In the final step the crystal structure of the HA receptor, the crystal structure of the Qβ capsid and the optimized linker structure are superimposed. All structure optimizations are performed with the Avogadro software[71] using the UFF force field.

5 Analytical Data

5.1 MST

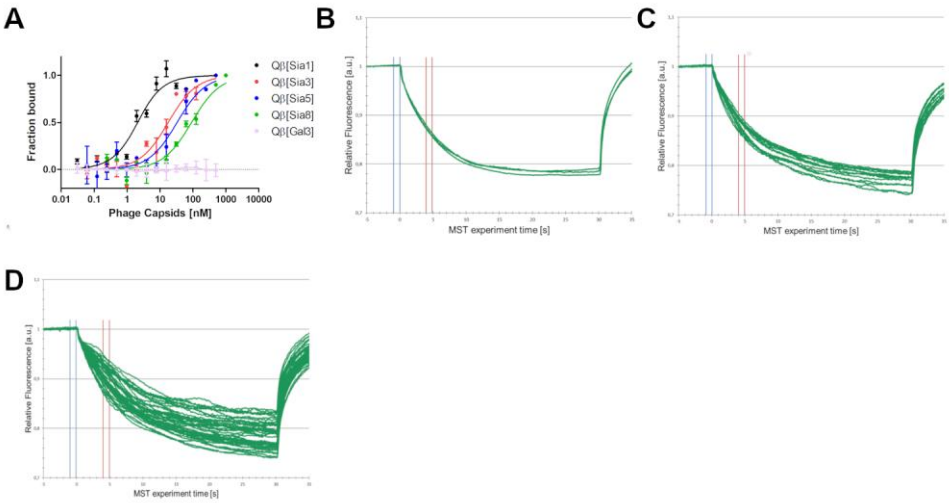

Fig. S 1: Microscale thermophoresis of octadecyl rhodamine B chloride (r18) labeled A/X31. (a) Binding curves from experiments with Qβ[Sia1,3,5,8] and the control Qβ[Gal3] towards X31. The errors indicate the SEM (N≥3) from independent dilution preparations (a), Change in fluorescence during thermophoresis from dilution series either of Qβ[Gal3] phage capsids against X31 (b), or Qβ[Sia1] phage capsids against X31 (c). Change in fluorescence was obtained from the difference between the indicated gates at the initial fluorescence (blue gate) before start of thermophoresis and 5 s after the start (red gate) within the thermophoresis process.

5.2 Qβ[Hpg]

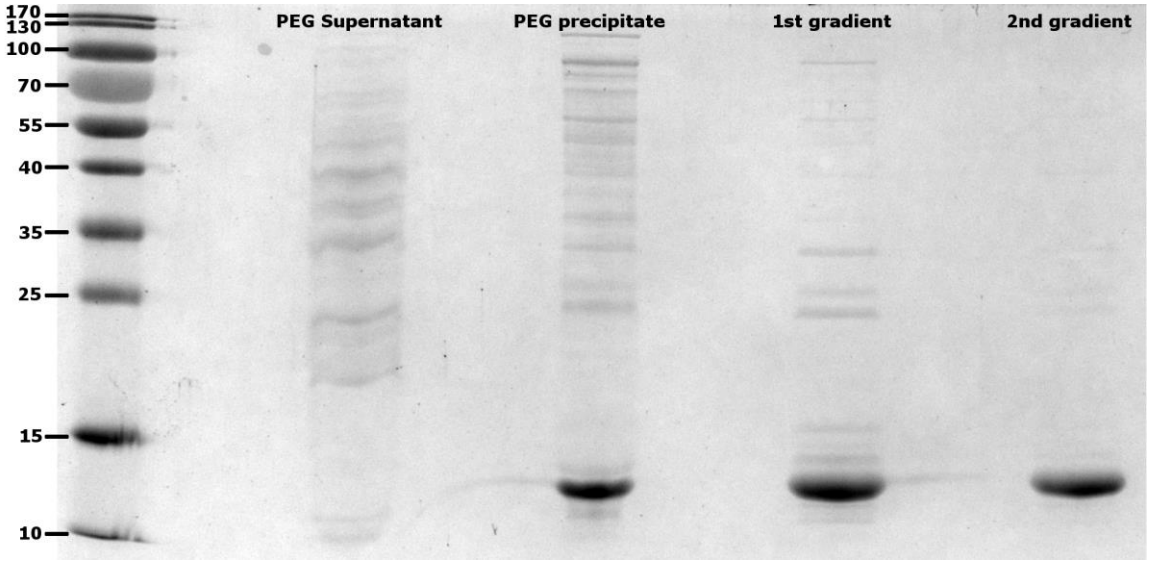

Fig. S 2: SDS-PAGE of the Qβ[Hpg] purification process.

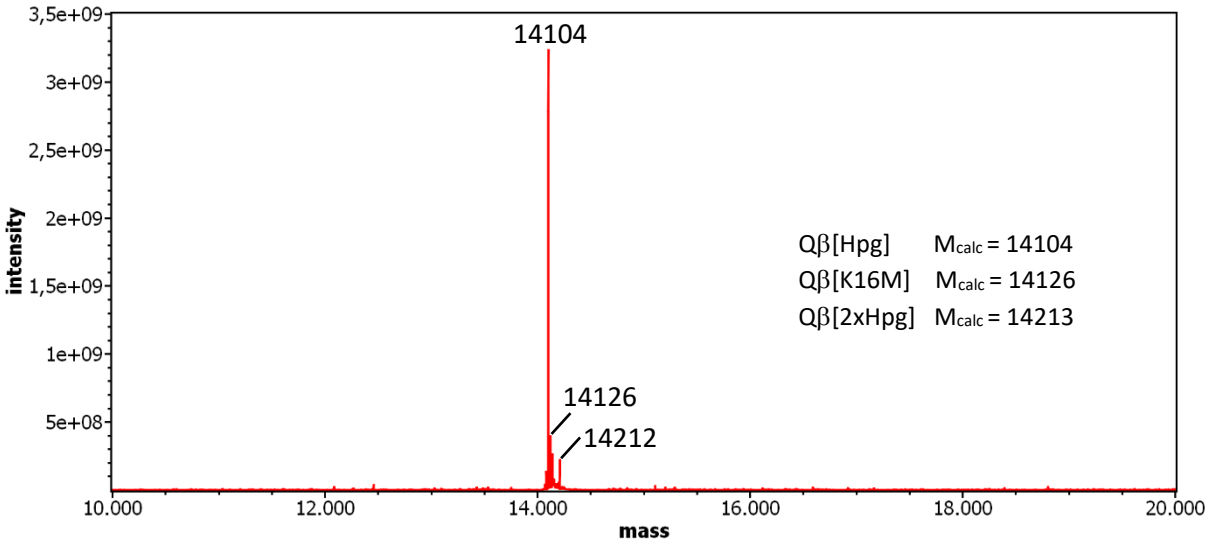

Fig. S 3: Deconvoluted ESI-MS spectrum of **Qβ[Hpg]**.

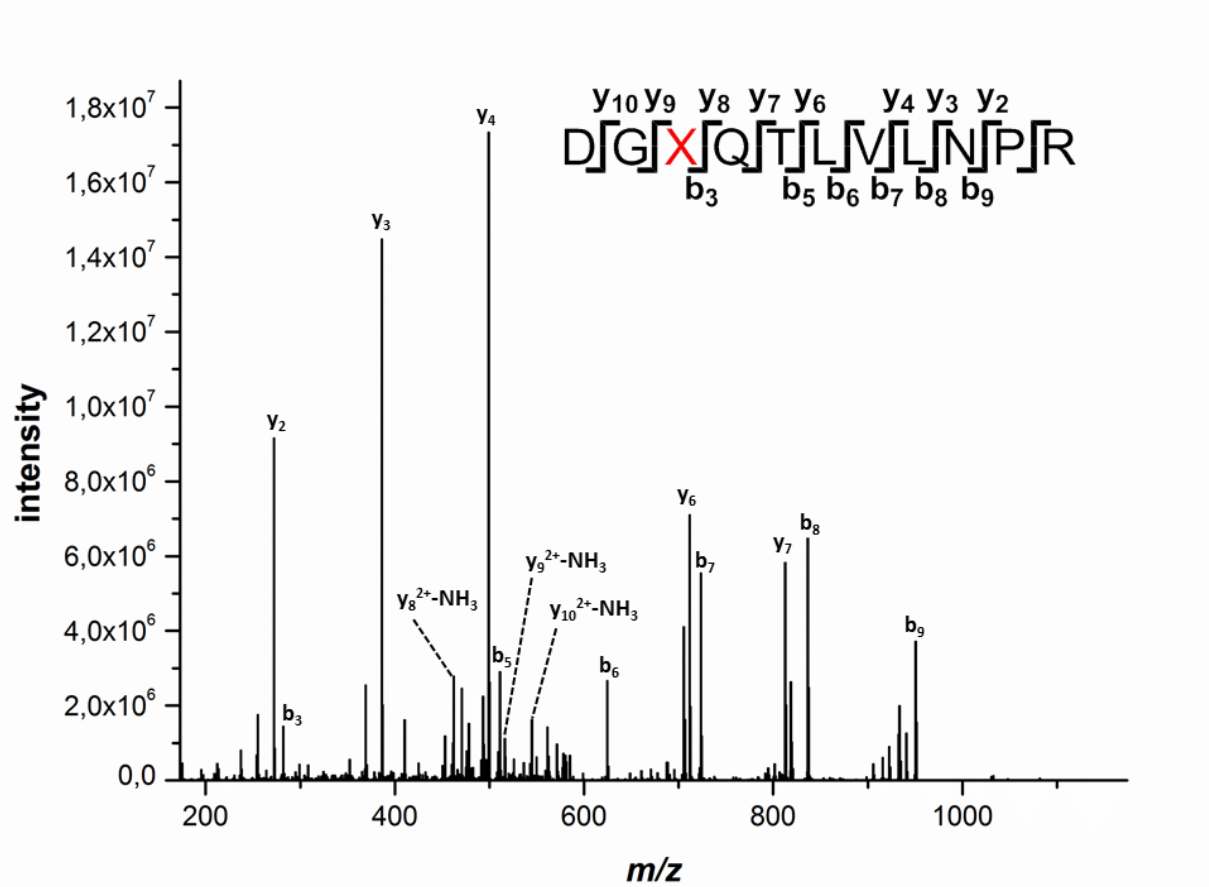

Fig. S 4: MS/MS Fragment spectrum of the diagnostic peptide that carries the incorporated Hpg at position 16 of the coat protein sequence.

5.3 Qβ[Gal3]

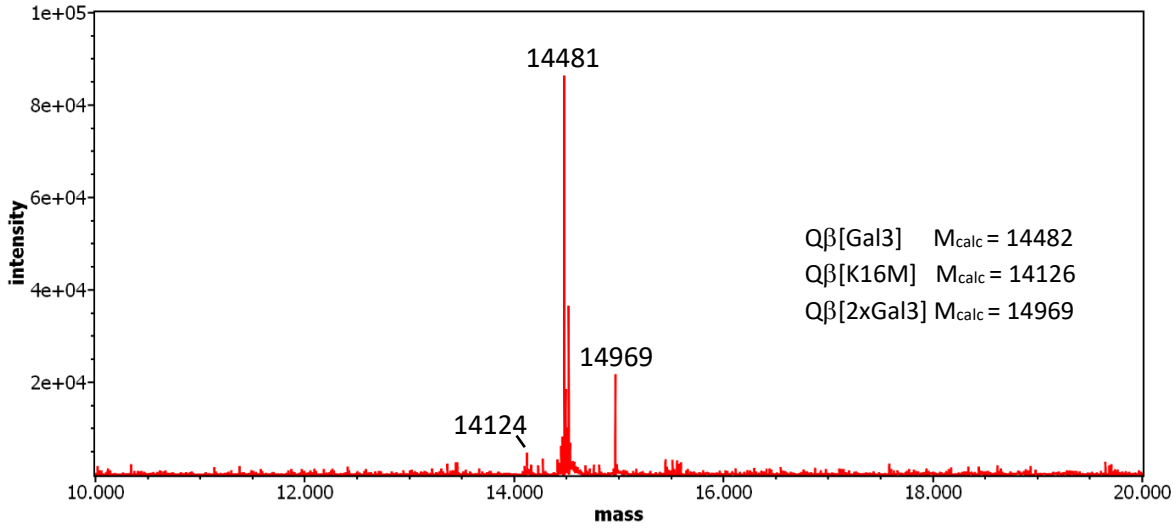

Fig. S 5: Deconvoluted ESI-MS spectrum of **Qβ[Gal3]**.

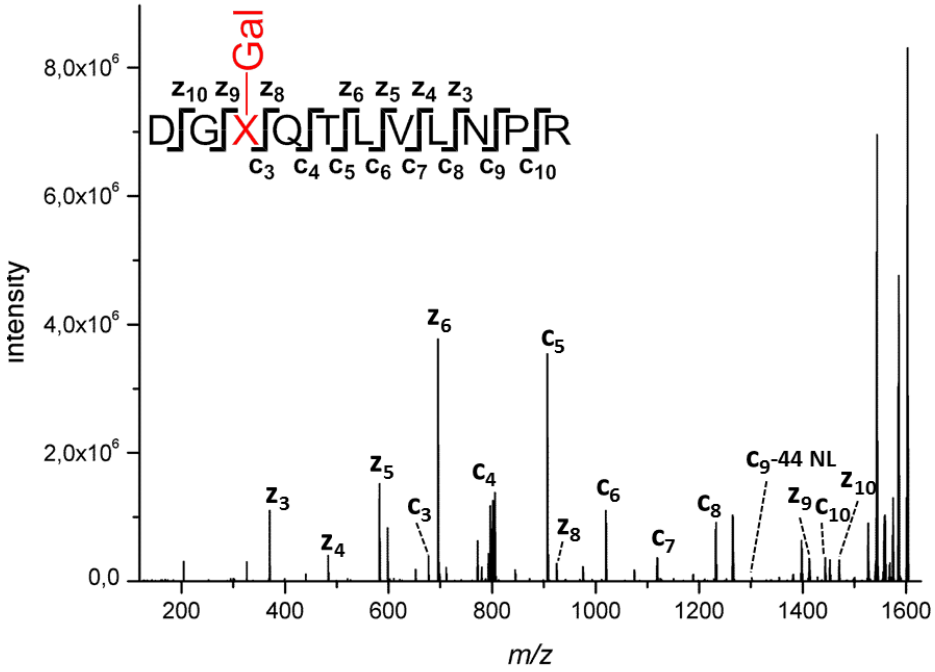

Fig. S 6: MS/MS Fragment spectrum of the diagnostic peptide that carries the desired Gal modification at position 16 of the coat protein sequence.

5.4 Qβ[Sia0]

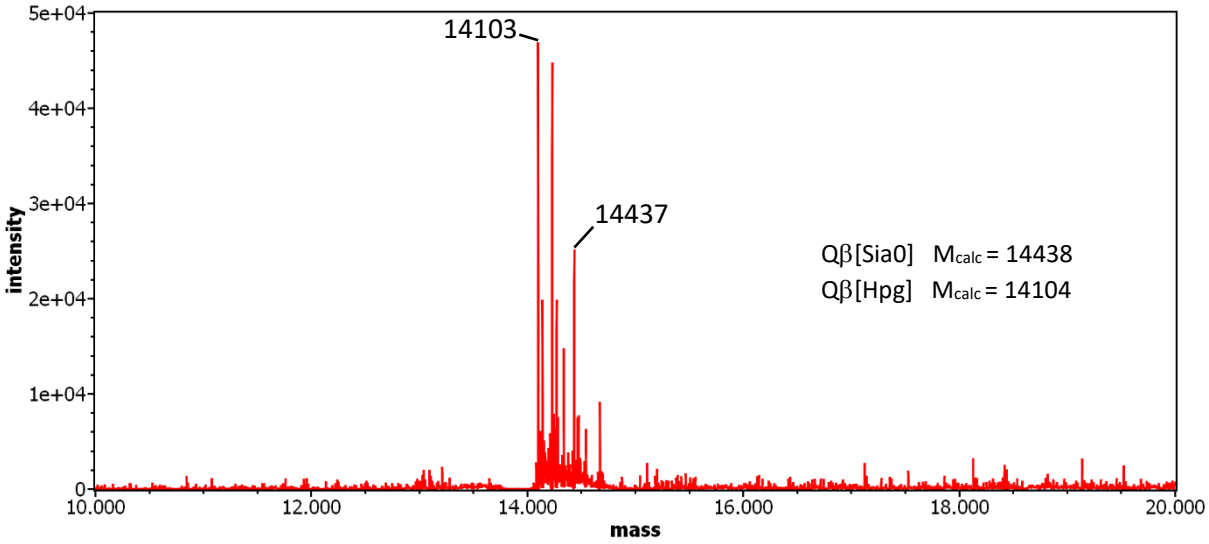

Fig. S 7: Deconvoluted ESI-MS spectrum of **Qβ[Sia0]**.

5.5 Qβ[Sia1]

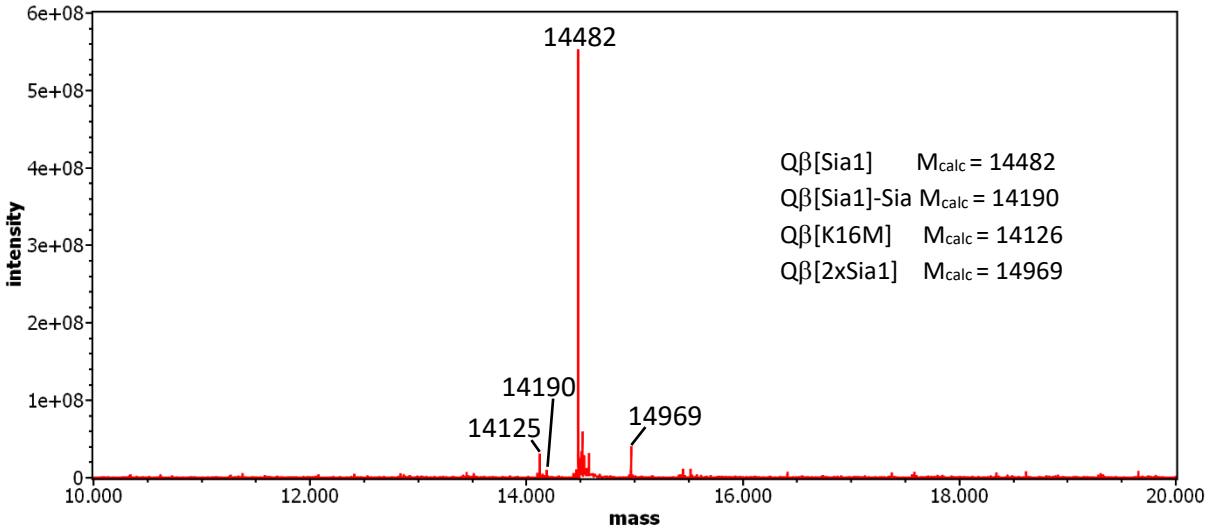

Fig. S 8. Deconvoluted ESI-MS spectrum of **Qβ[Sia1]**.

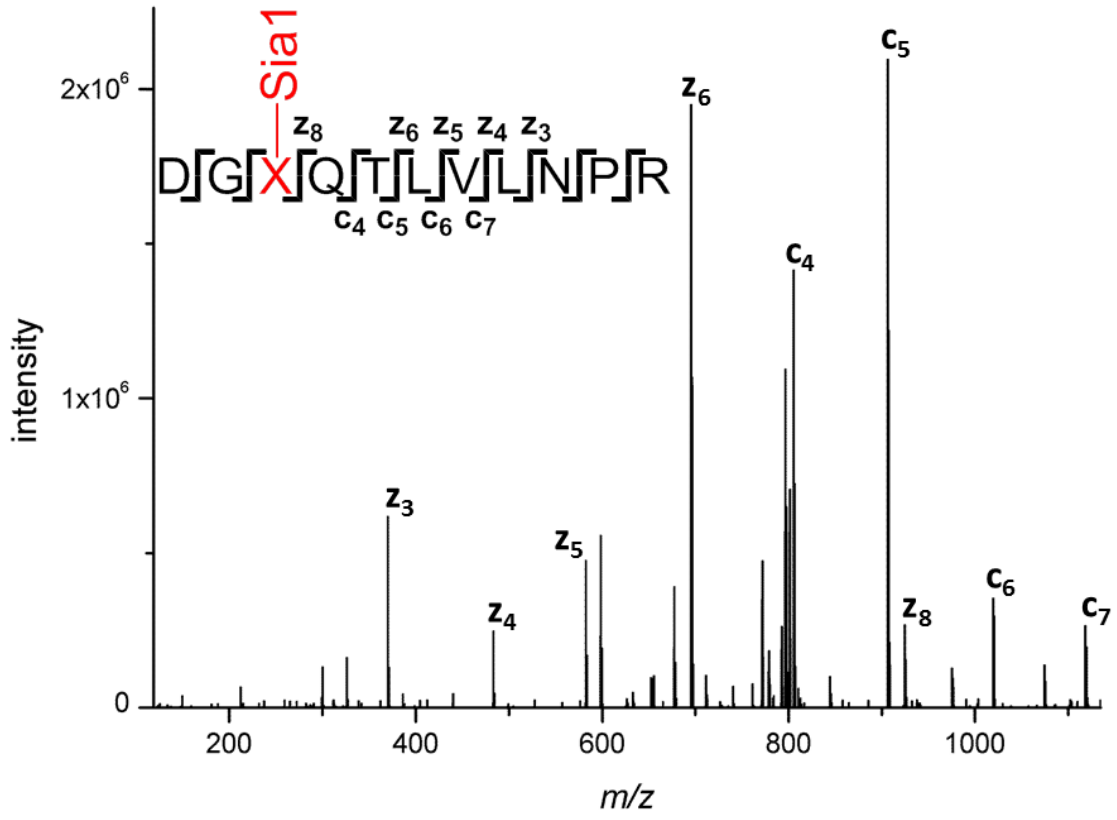

Fig. S 9: MS/MS Fragment spectrum of the diagnostic peptide that carries the desired Sia1 modification at position 16 of the coat protein sequence.

5.6 Qβ[Sia3]

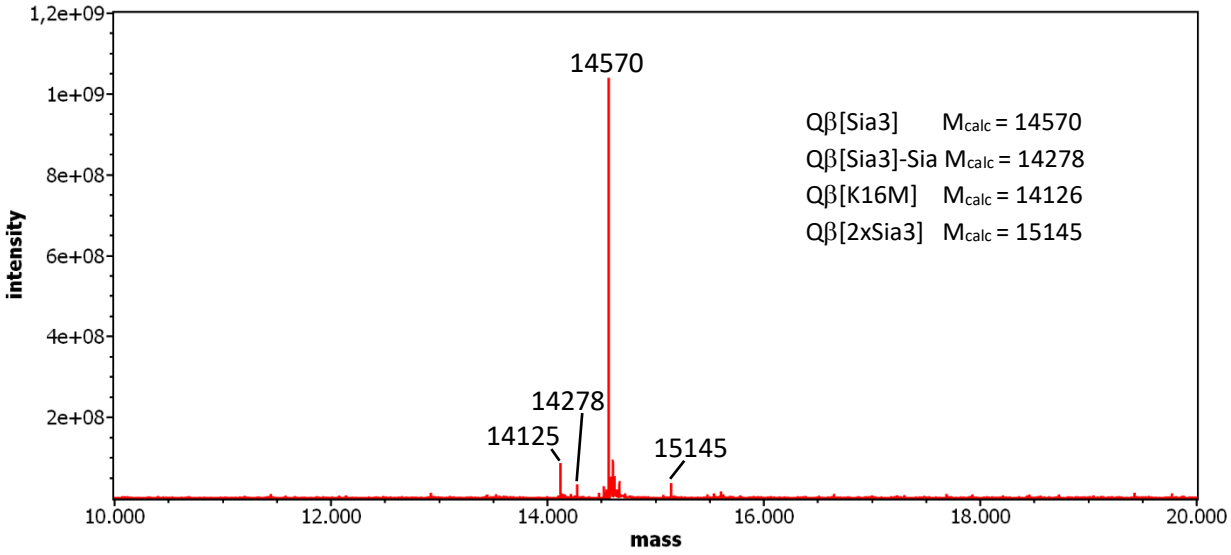

Fig. S 10: Deconvoluted ESI-MS spectrum of **Qβ[Sia3]**.

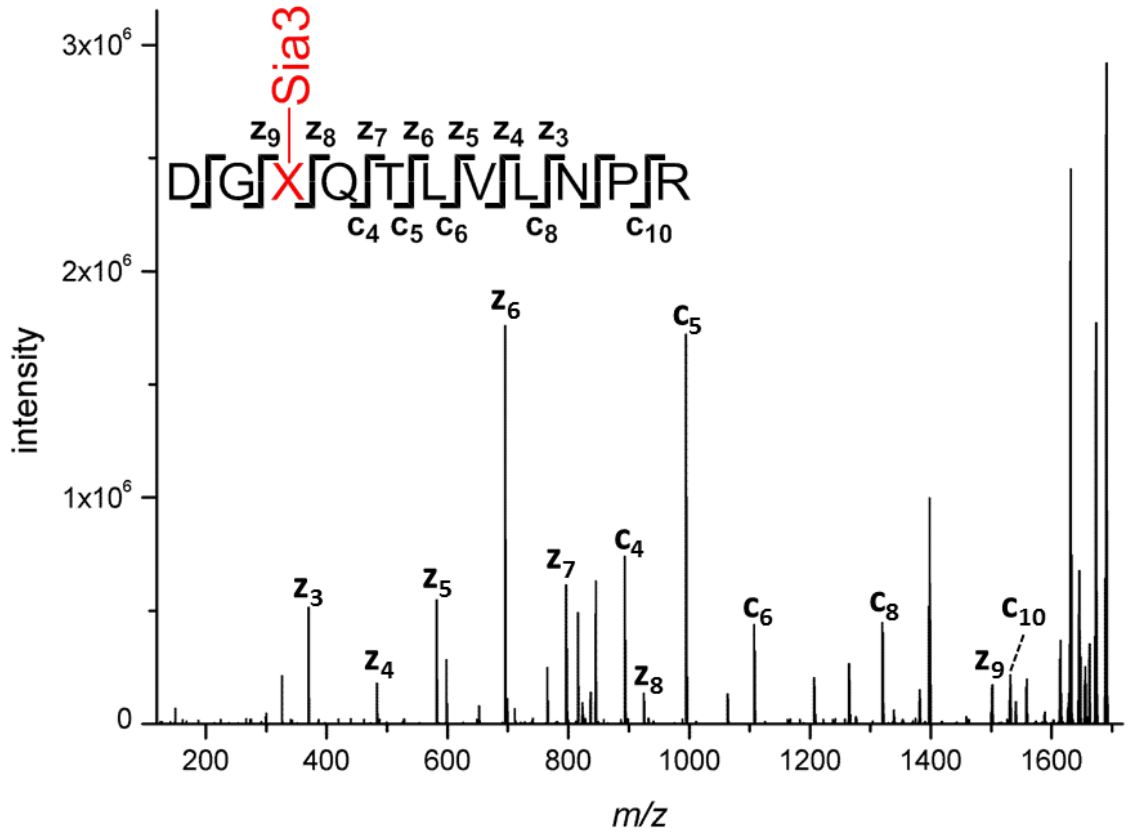

Fig. S 11: MS/MS Fragment spectrum of the diagnostic peptide that carries the desired Sia3 modification at position 16 of the coat protein sequence.

5.7 Qβ[Sia5]

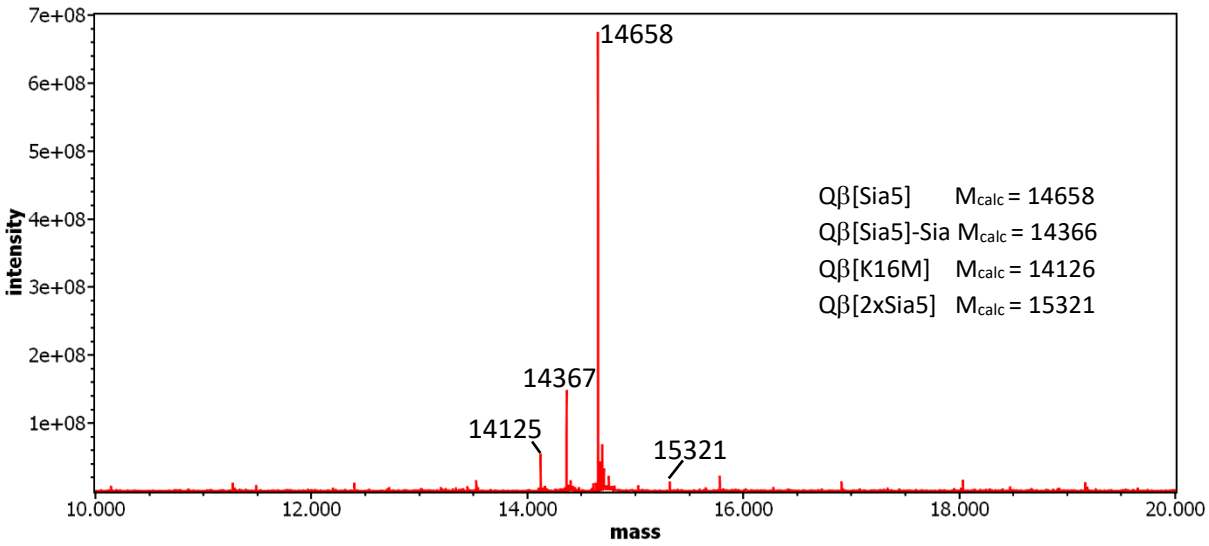

Fig. S 12: Deconvoluted ESI-MS spectrum of **Qβ[Sia5]**.

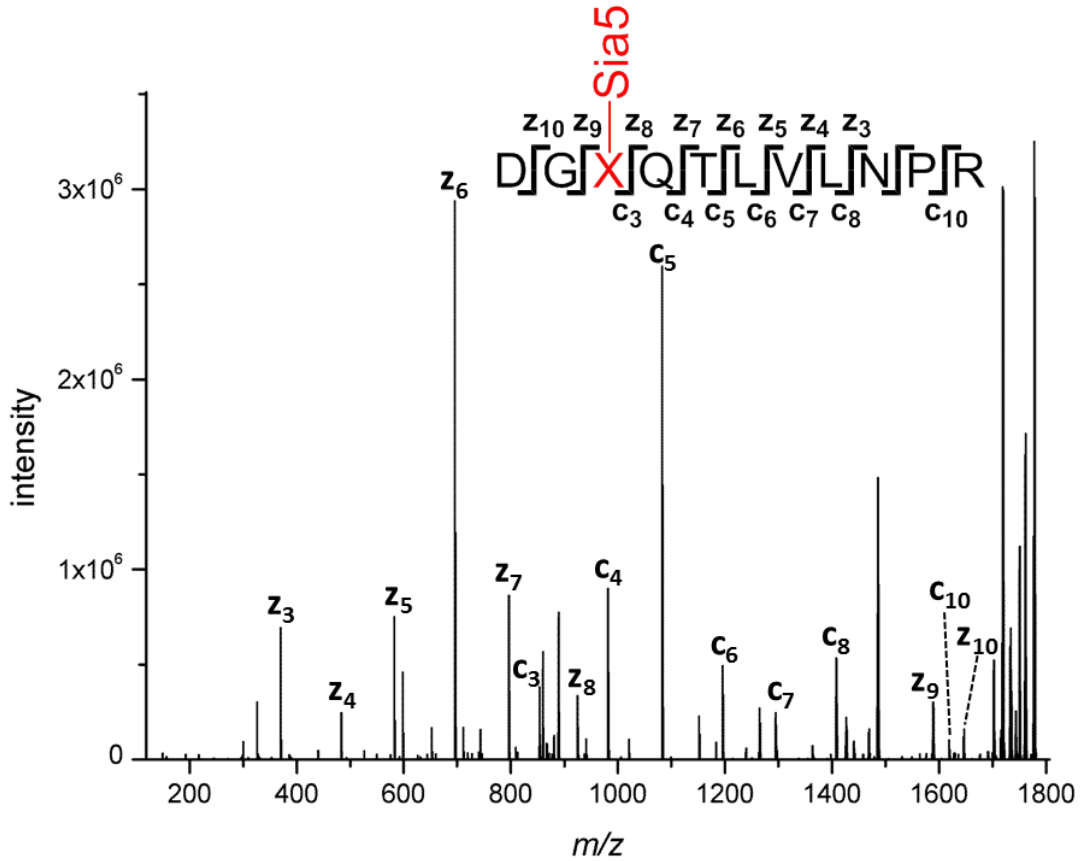

Fig. S 13: MS/MS Fragment spectrum of the diagnostic peptide that carries the desired Sia5 modification at position 16 of the coat protein sequence.

5.8 Qβ[Sia8]

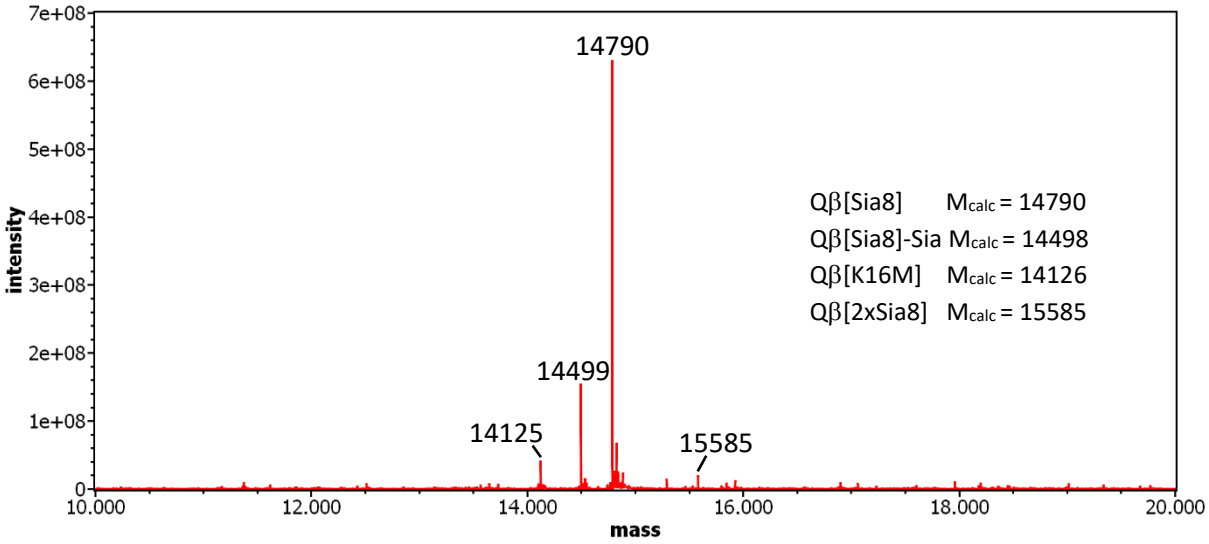

Fig. S 14: Deconvoluted ESI-MS spectrum of **Qβ[Sia8]**.

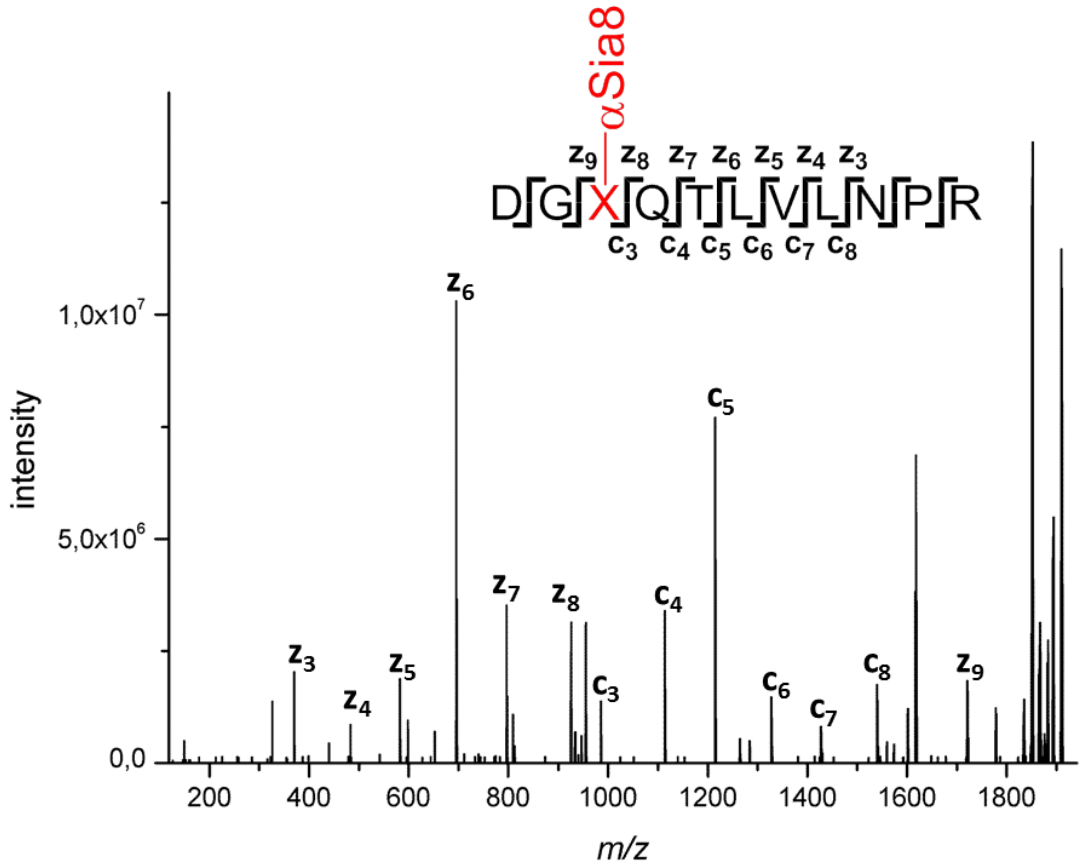

Fig. S 15: MS/MS Fragment spectrum of the diagnostic peptide that carries the desired Sia8 modification at position 16 of the coat protein sequence.

5.9 Qβ[2.6SL]

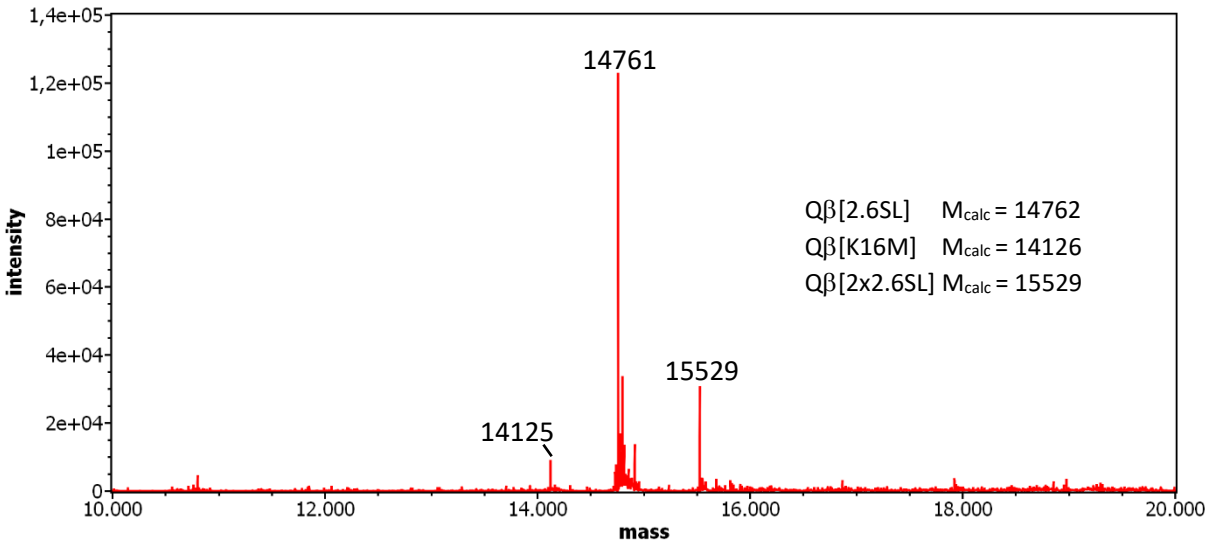

Fig. S 16: Deconvoluted ESI-MS spectrum of **Qβ[2.6SL]**.

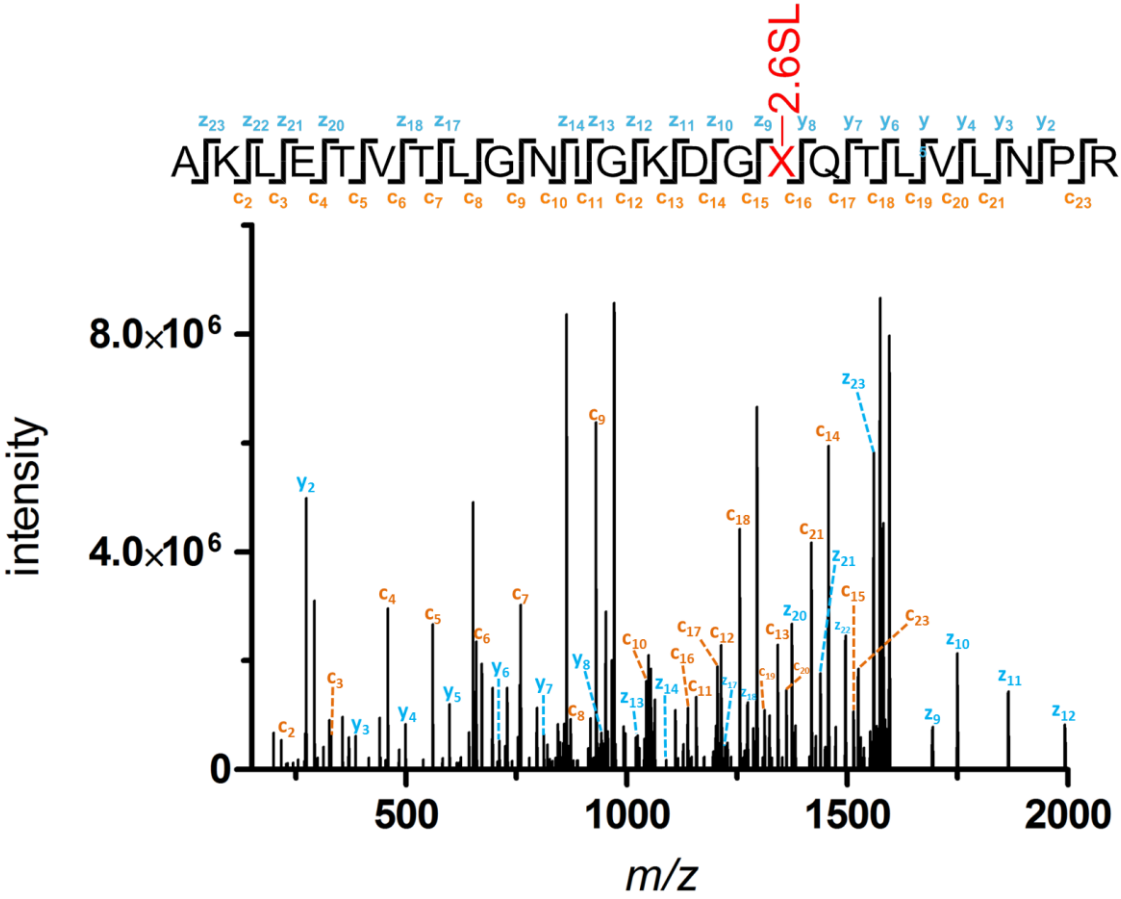

Fig. S 17: MS/MS Fragment spectrum of the diagnostic peptide that carries the desired 2.6SL modification at position 16 of the coat protein sequence.

5.10 Qβ[2.3SL]

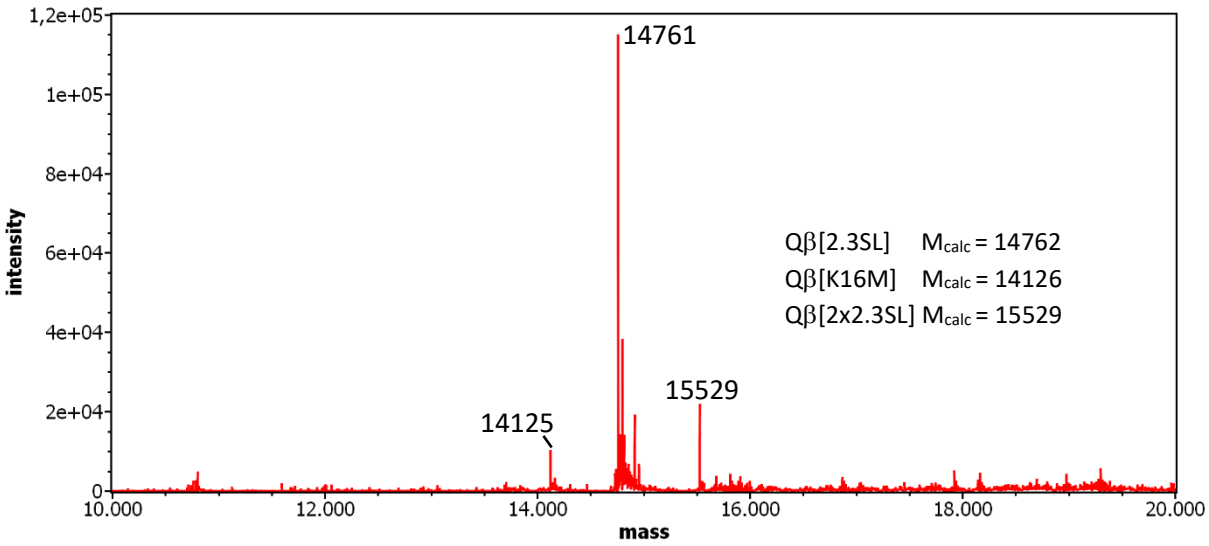

Fig. S 18: Deconvoluted ESI-MS spectrum of **Qβ[2.3SL]**.

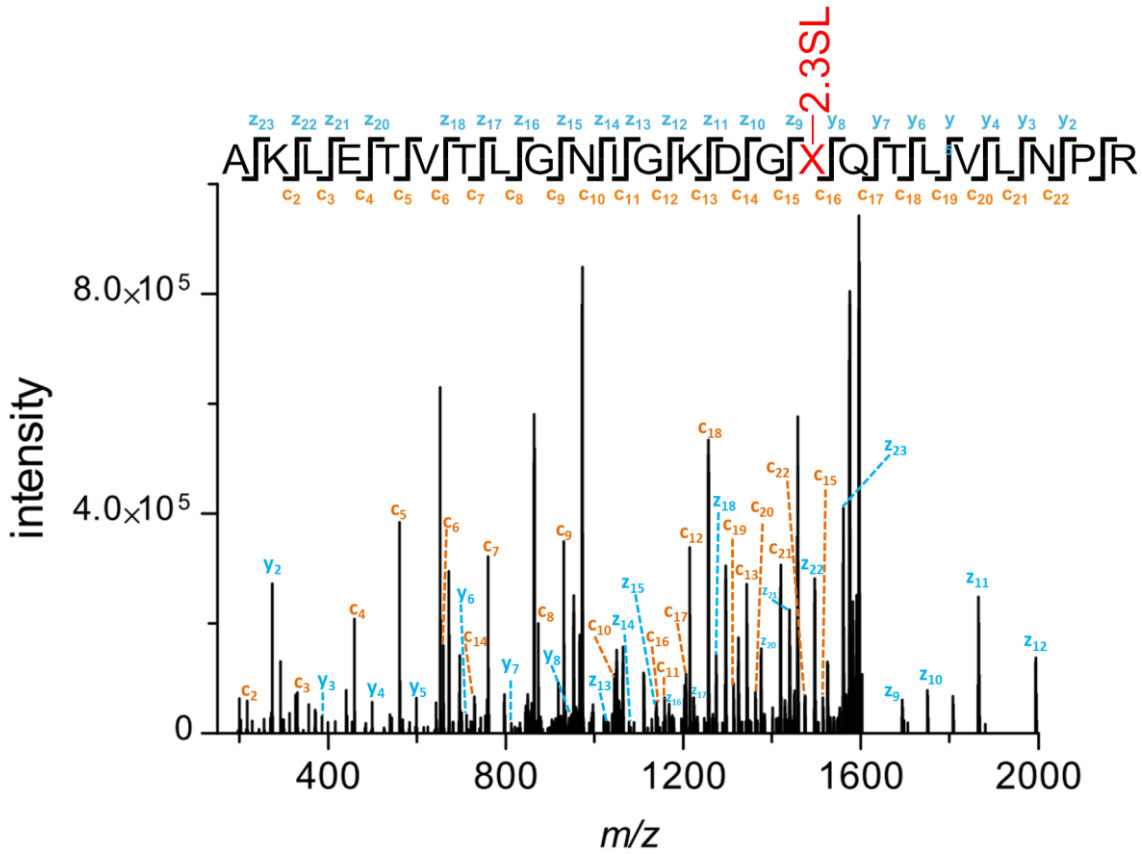

Fig. S 19: MS/MS Fragment spectrum of the diagnostic peptide that carries the desired 2.3SL modification at position 16 of the coat protein sequence.

5.11 NMR spectra

^{1}H-NMR of **Gal3** (300 MHz, D_2O):

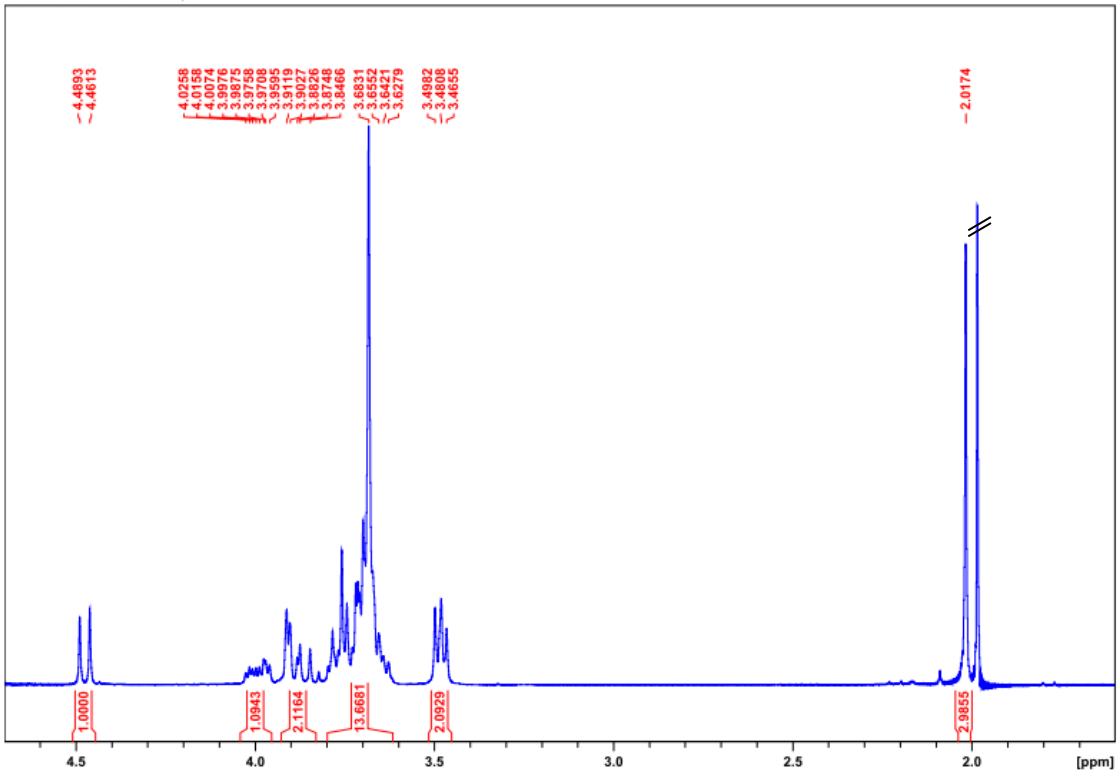

^{13}C-NMR of **Gal3** (75 MHz, D_2O):

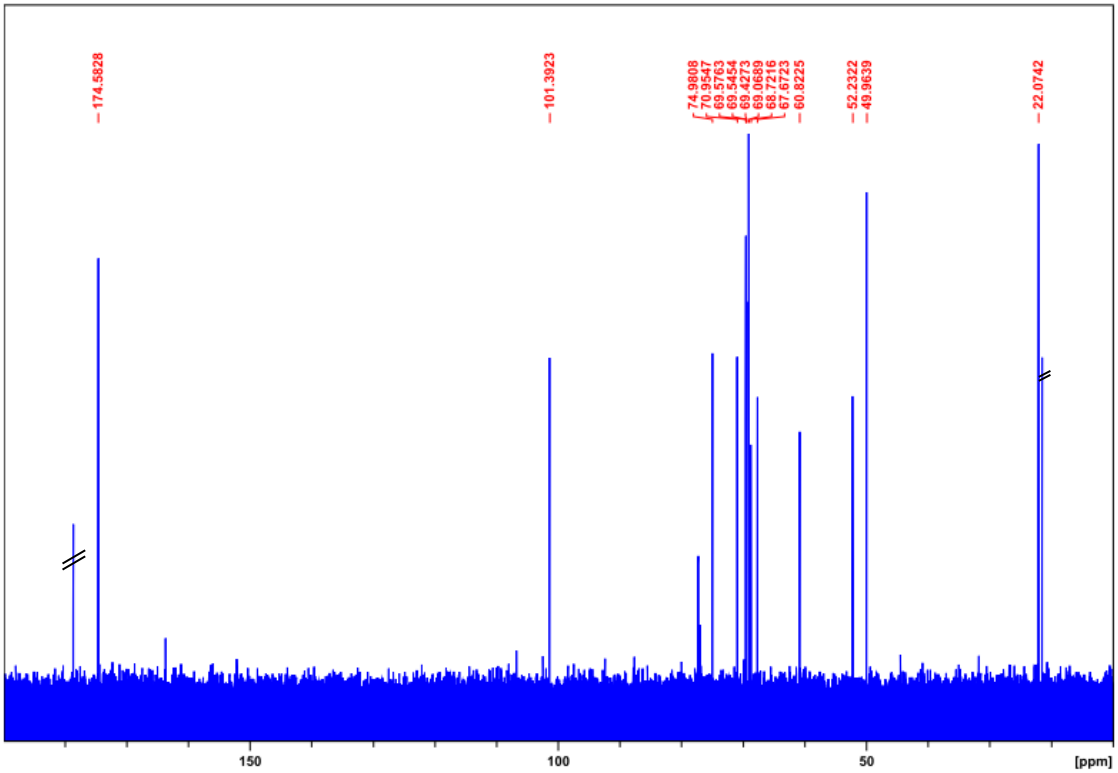

^{1}H-NMR of **Sia0** (300 MHz, D_2O):

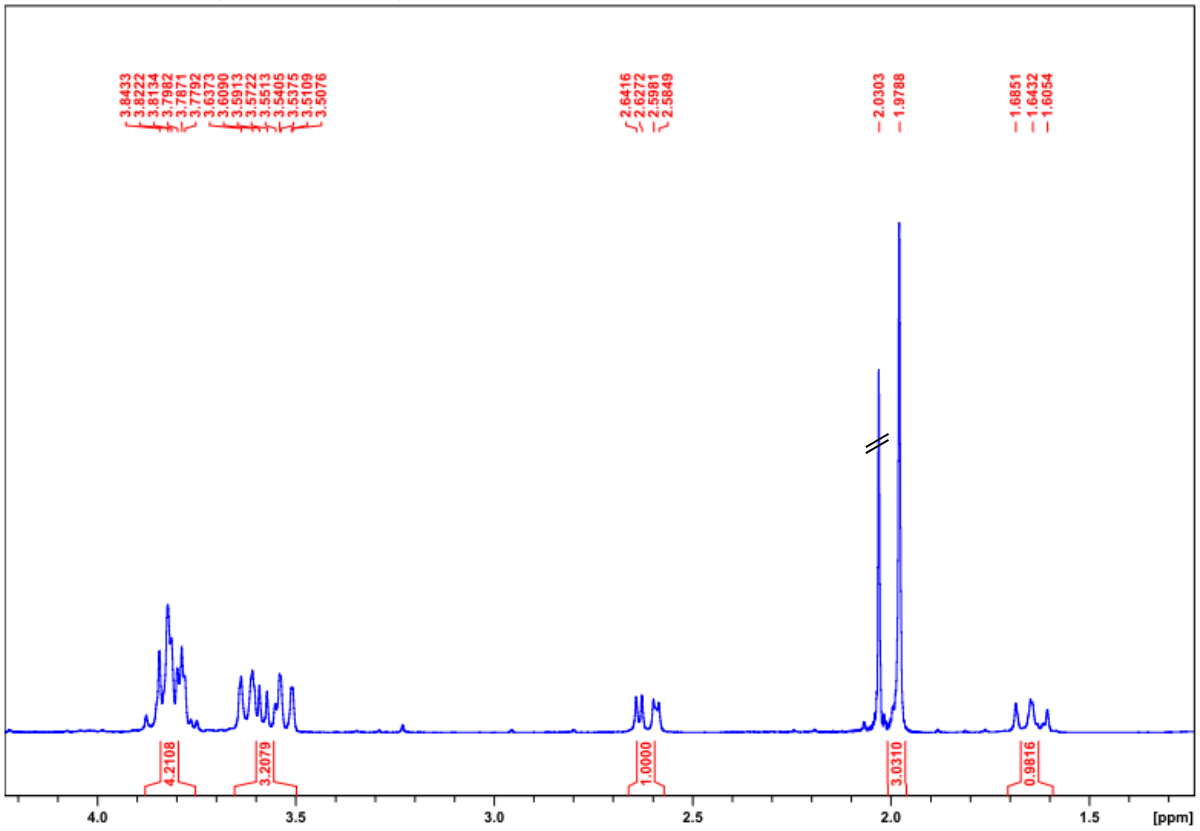

^{13}C-NMR of **Sia0** (75 MHz, D_2O):

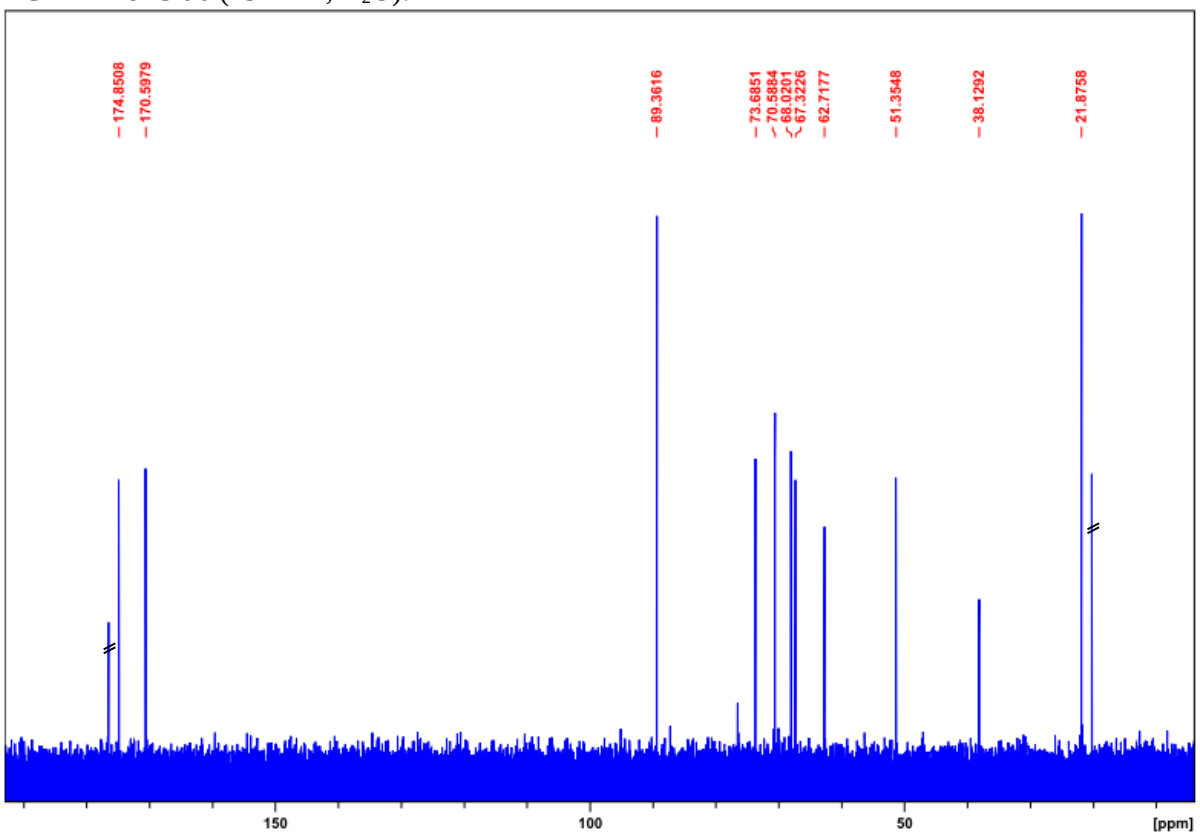

^{1}H-NMR of **AcSia1** (300 MHz, $CDCl_3$):

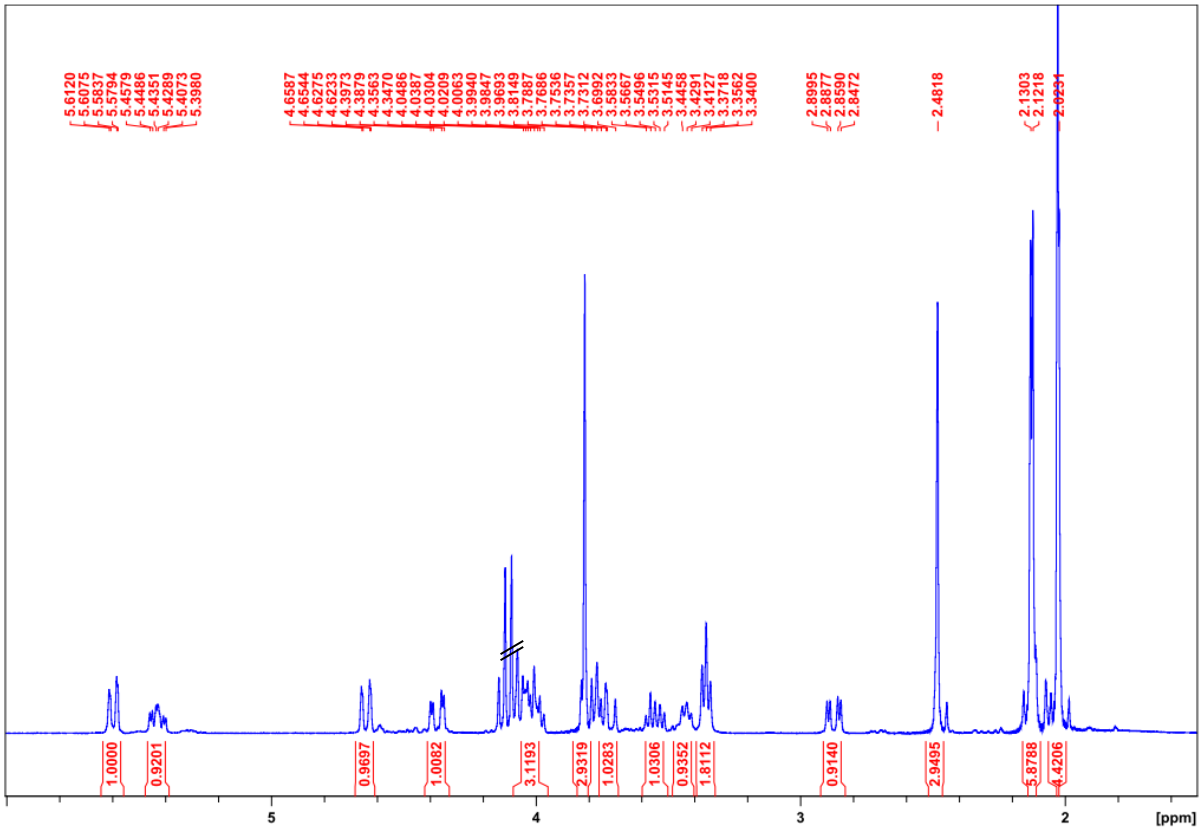

^{13}C-NMR of **AcSia1** (75 MHz, $CDCl_3$):

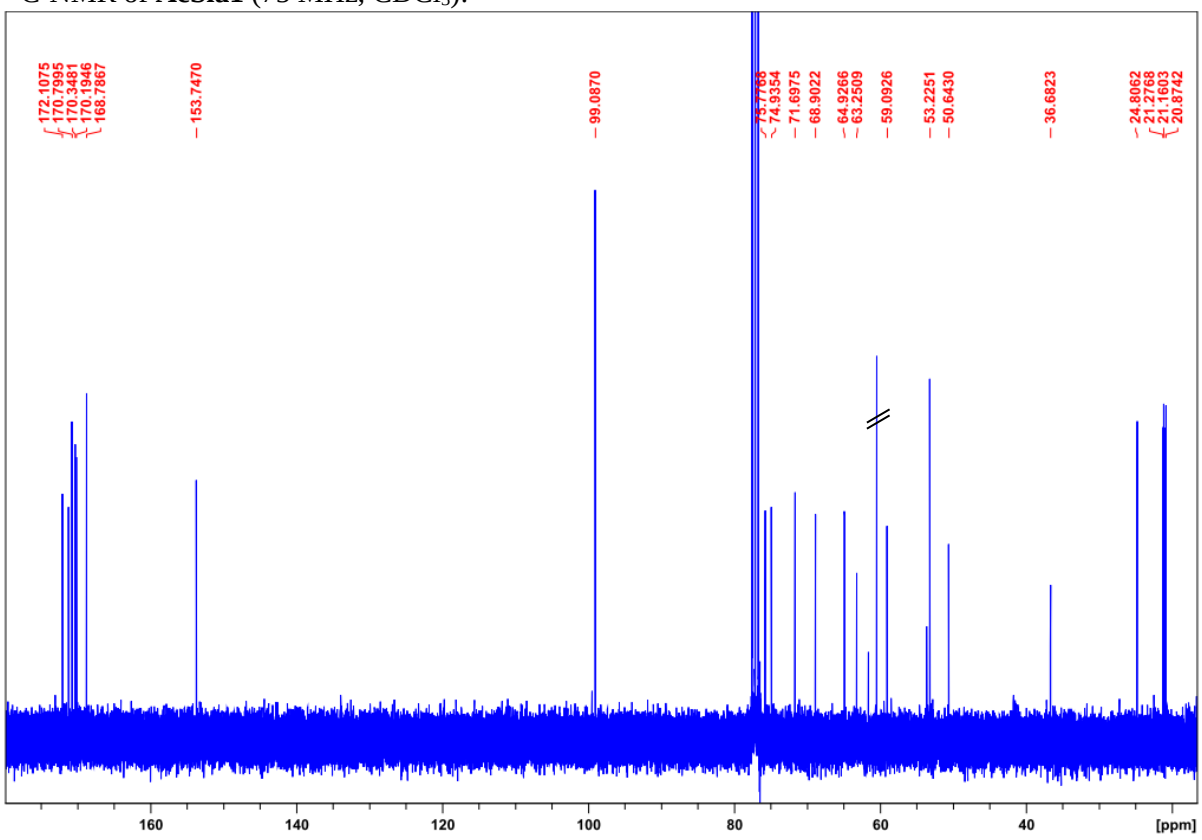

^{1}H-NMR of **Sia1** (300 MHz, D_2O):

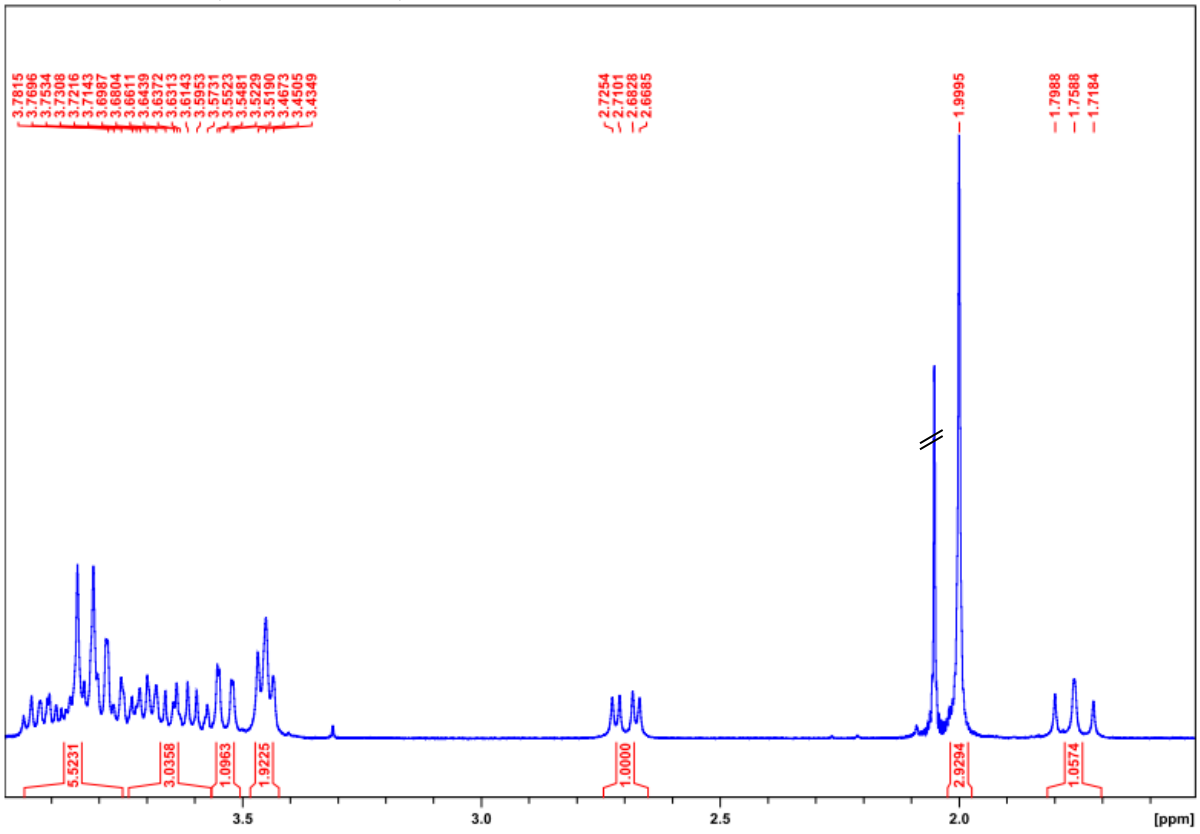

^{13}C-NMR of **Sia1** (75 MHz, D_2O):

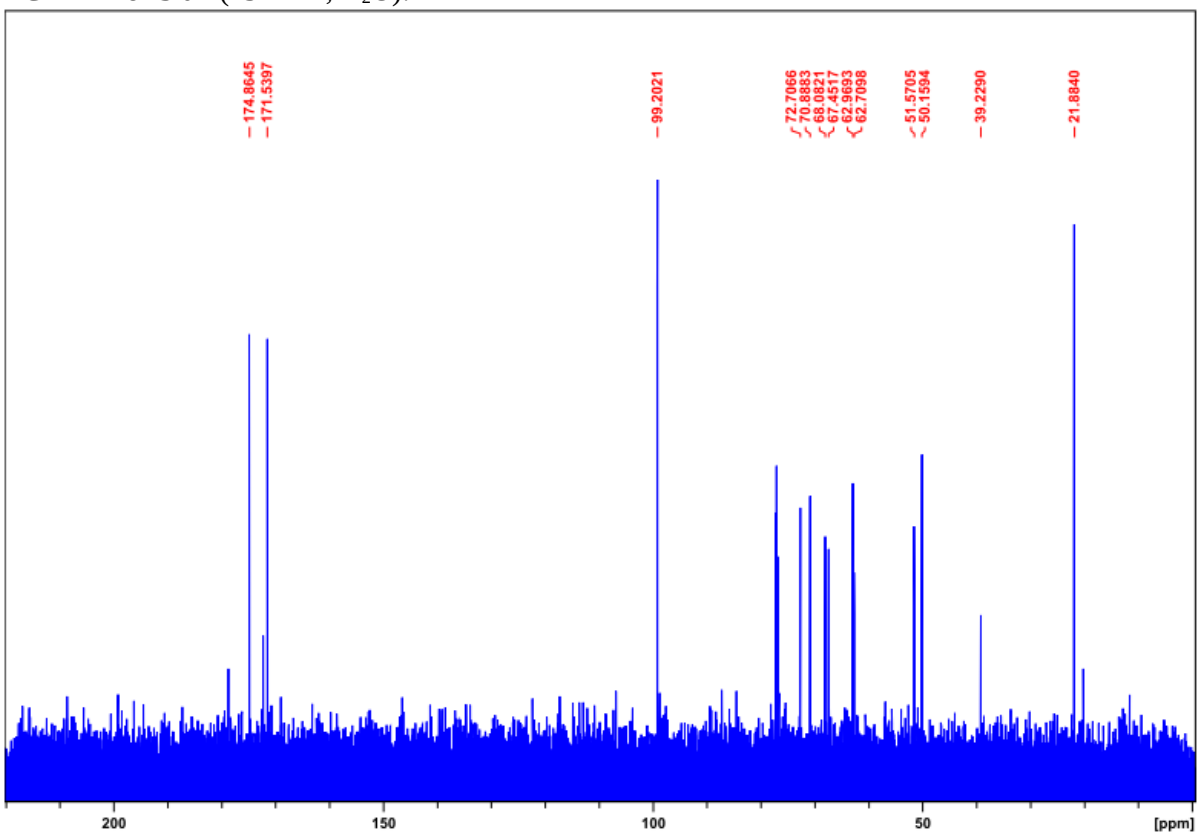

^{1}H-NMR of **AcSia3** (300 MHz, $CDCl_3$):

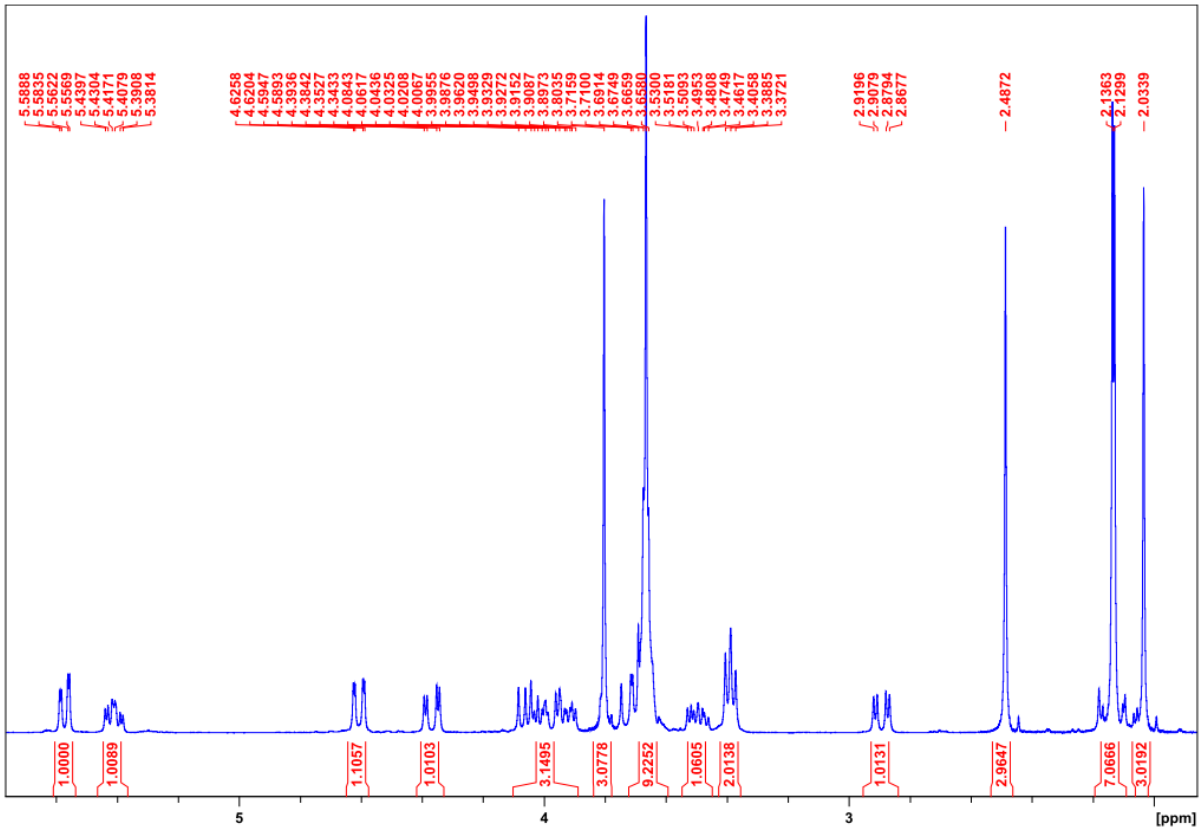

^{13}C-NMR of **AcSia3** (75 MHz, $CDCl_3$):

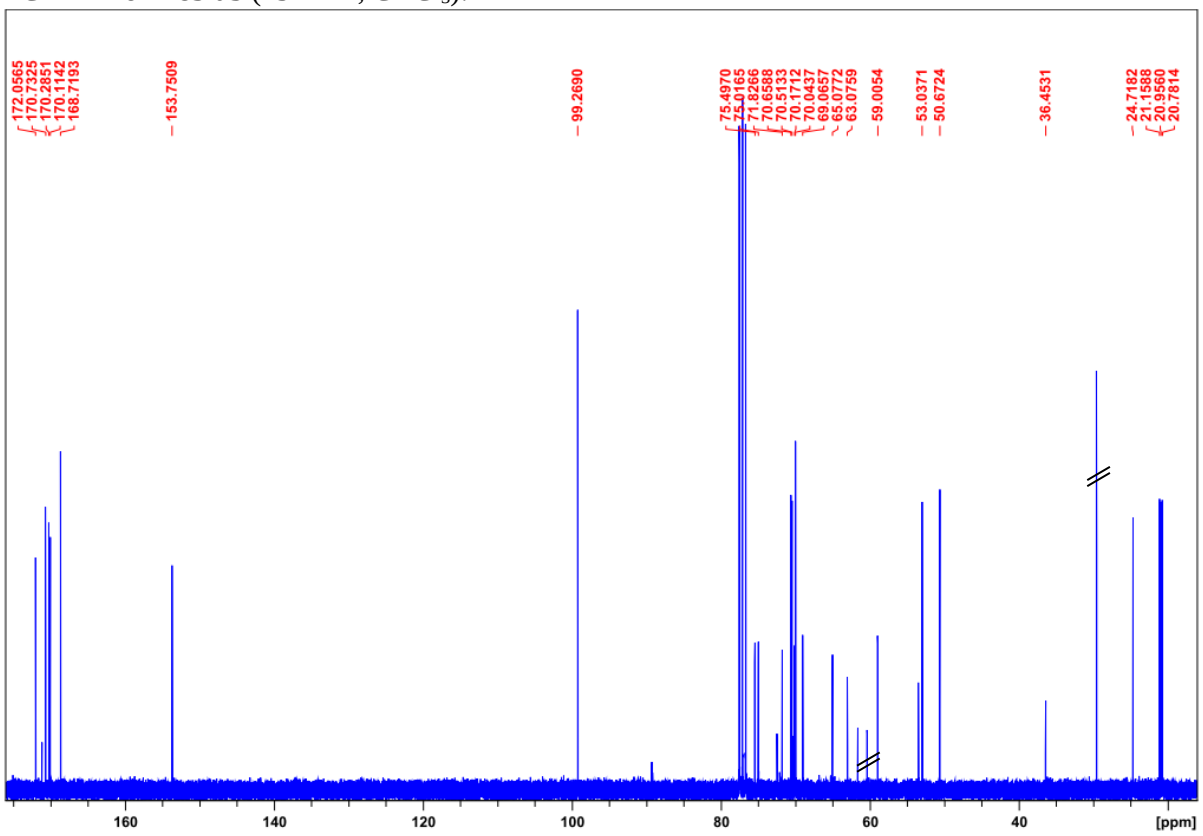

^{1}H-NMR of **Sia3** (300 MHz, D_2O):

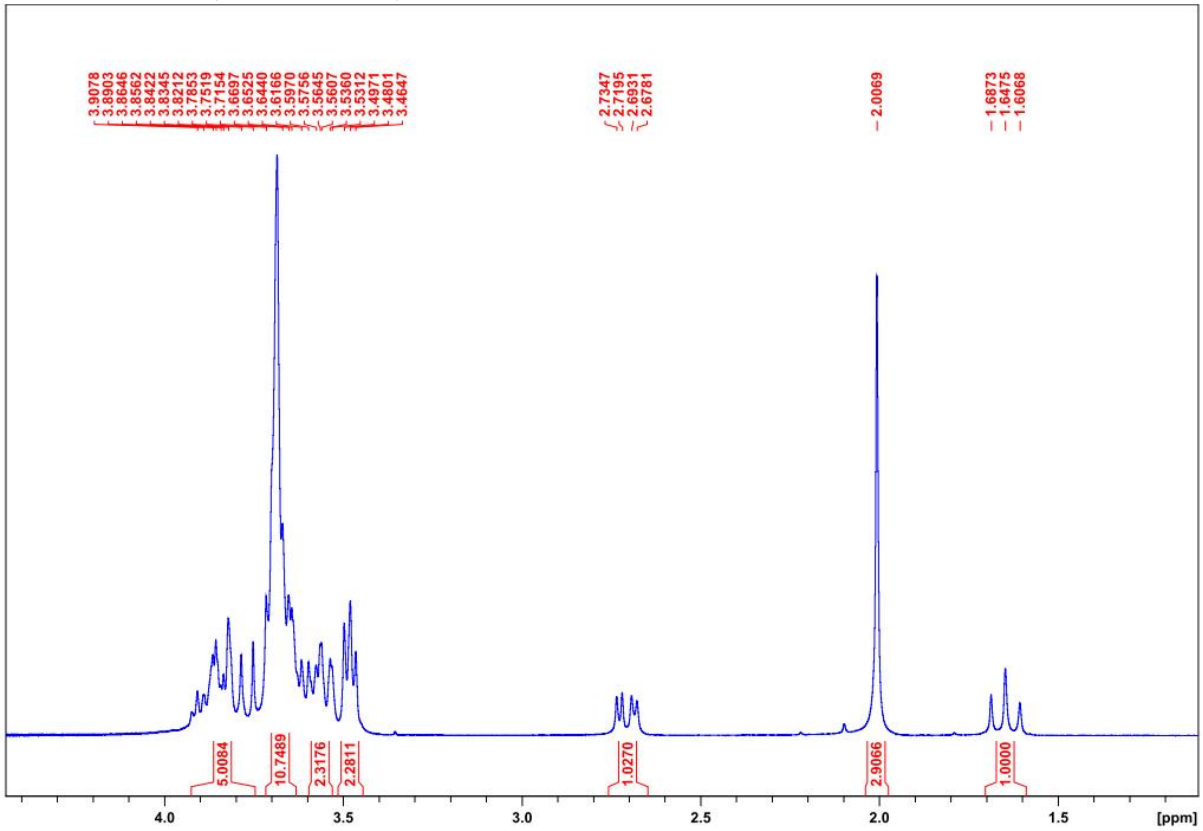

^{13}C-NMR of **Sia3** (75 MHz, D_2O):

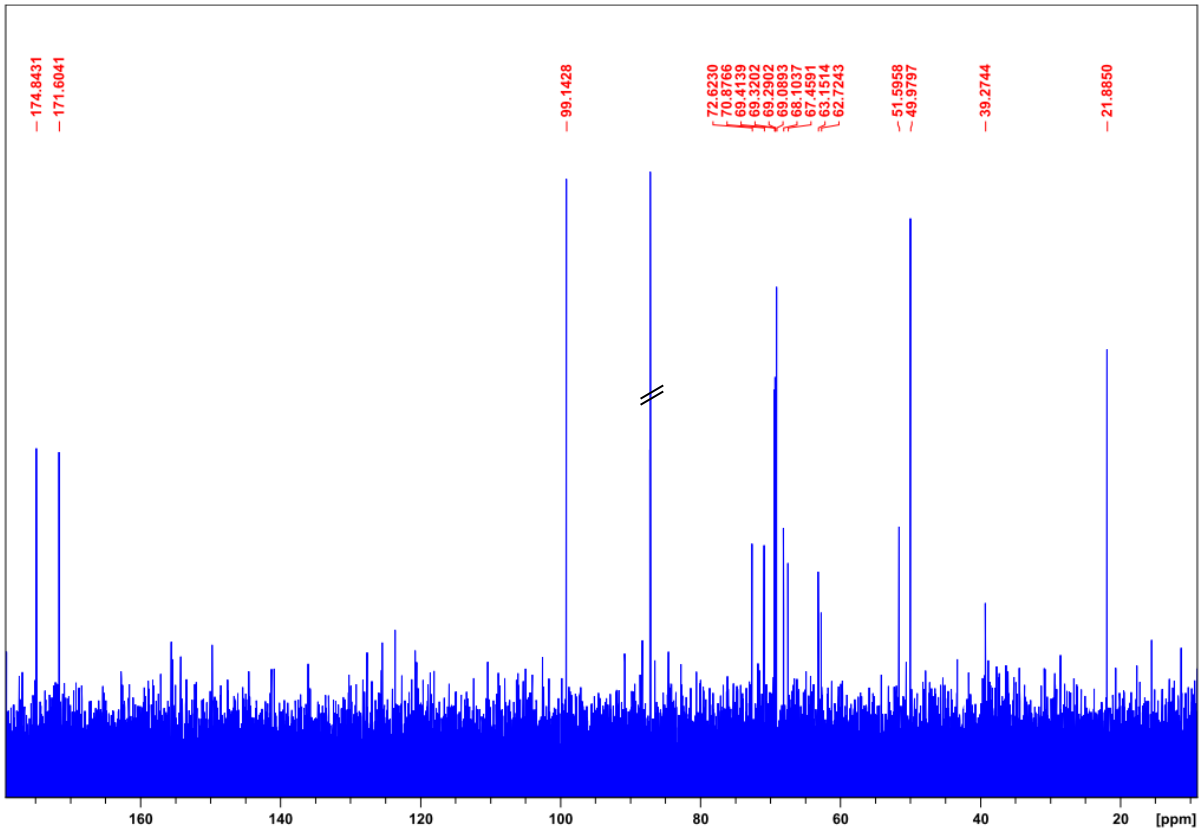

^{1}H-NMR of **AcSia5** (300 MHz, $CDCl_3$):

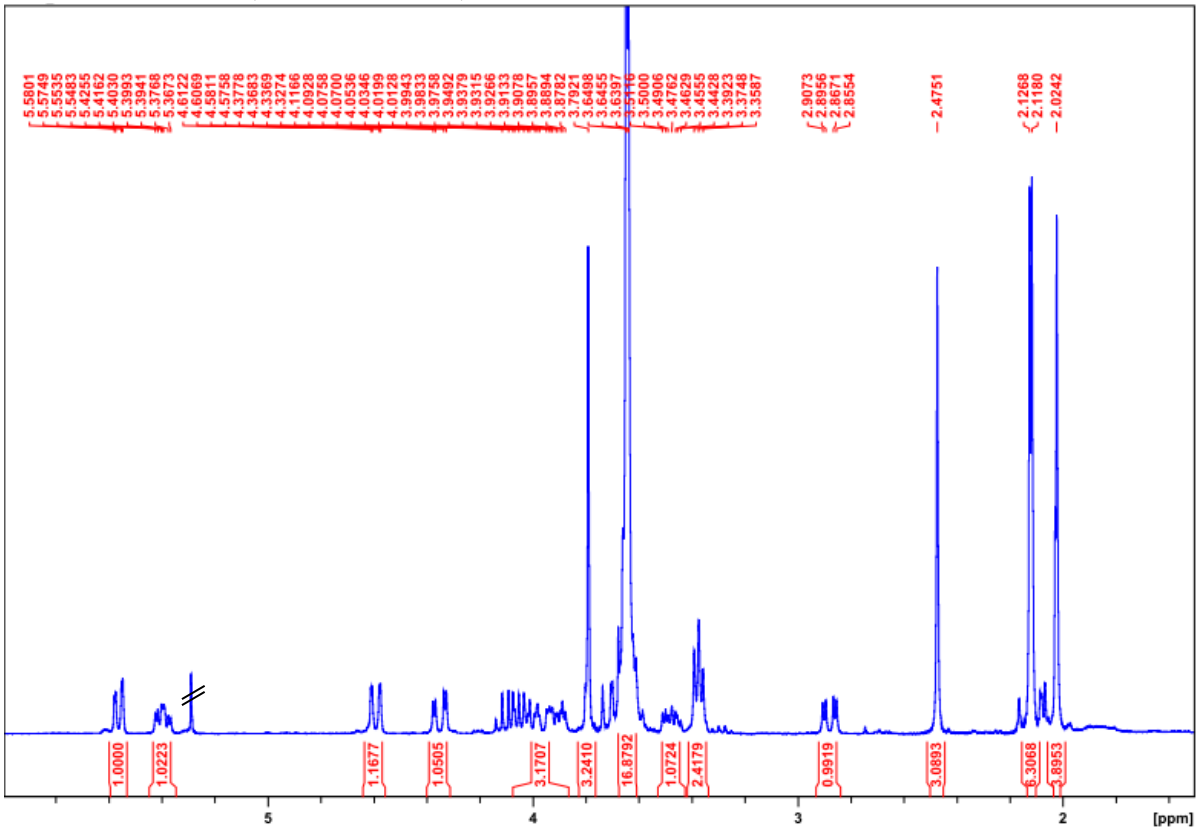

^{13}C-NMR of **AcSia5** (75 MHz, $CDCl_3$):

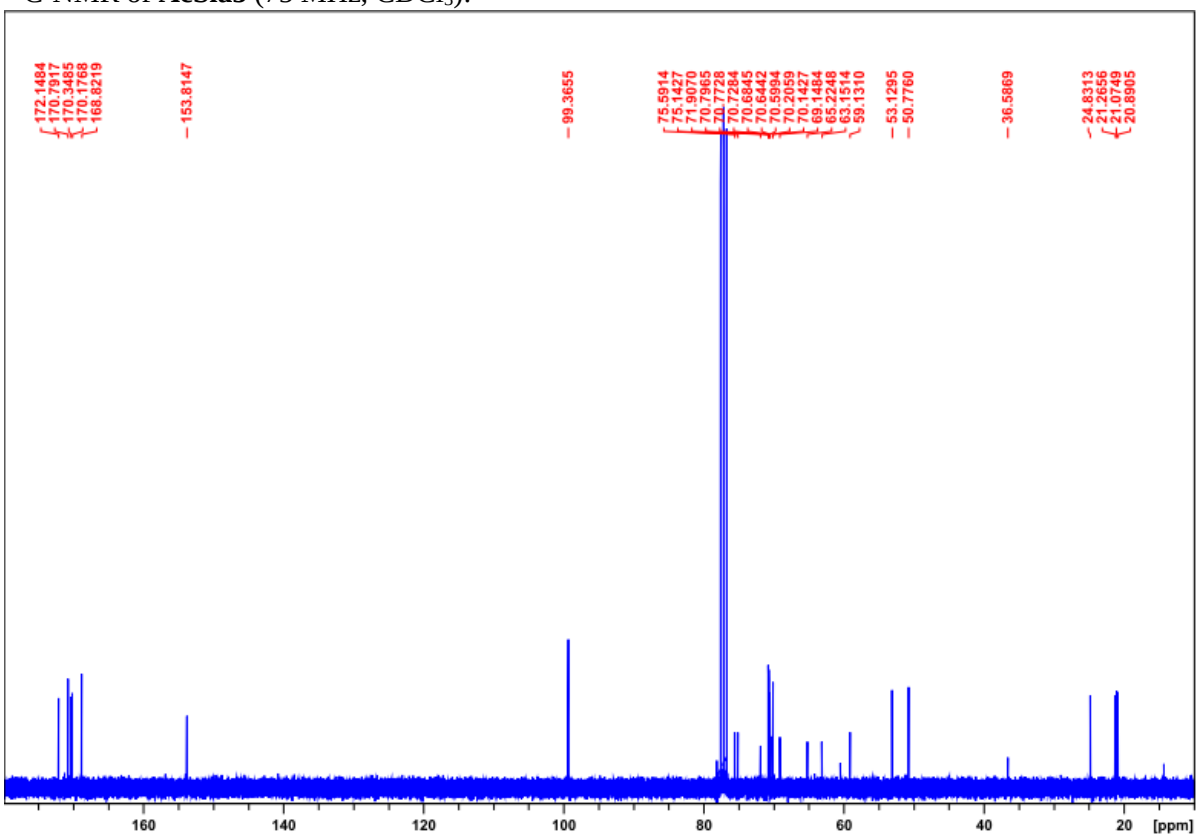

^{1}H-NMR of **Sia5** (300 MHz, D_2O):

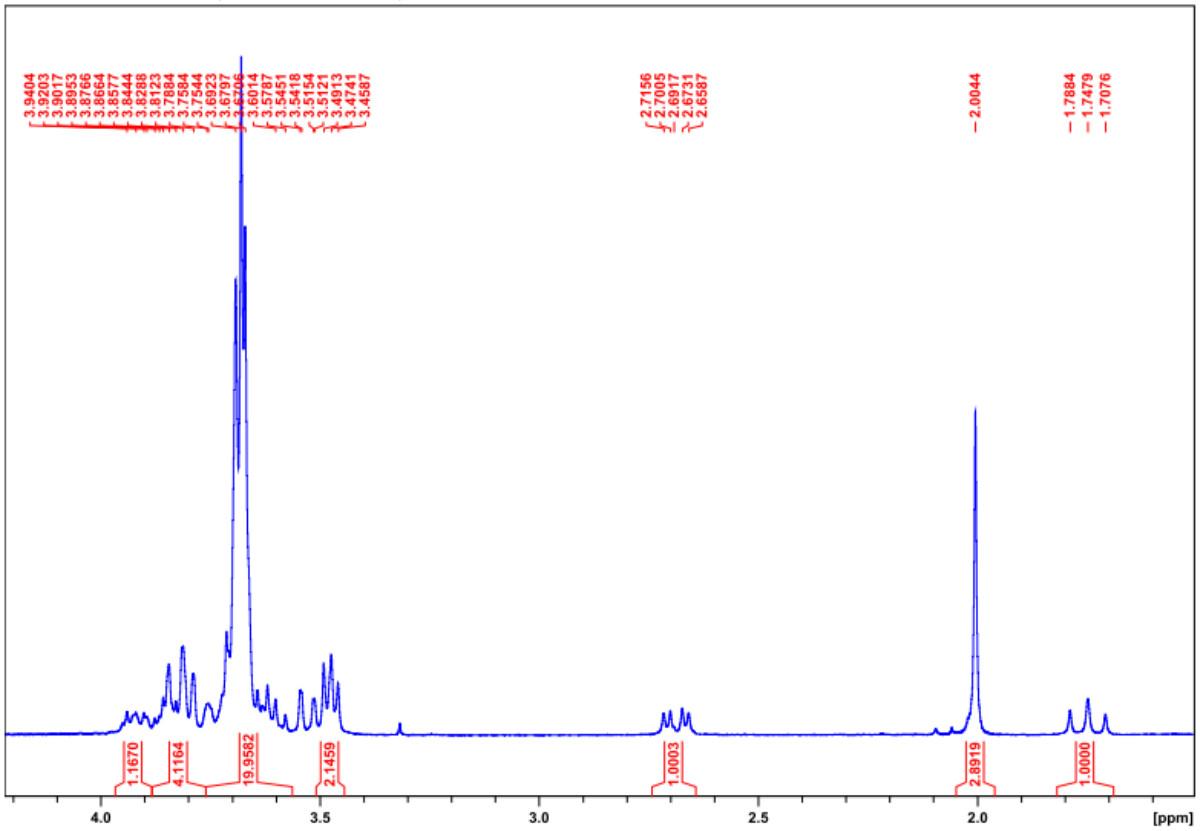

^{13}C-NMR of **Sia5** (75 MHz, D_2O):

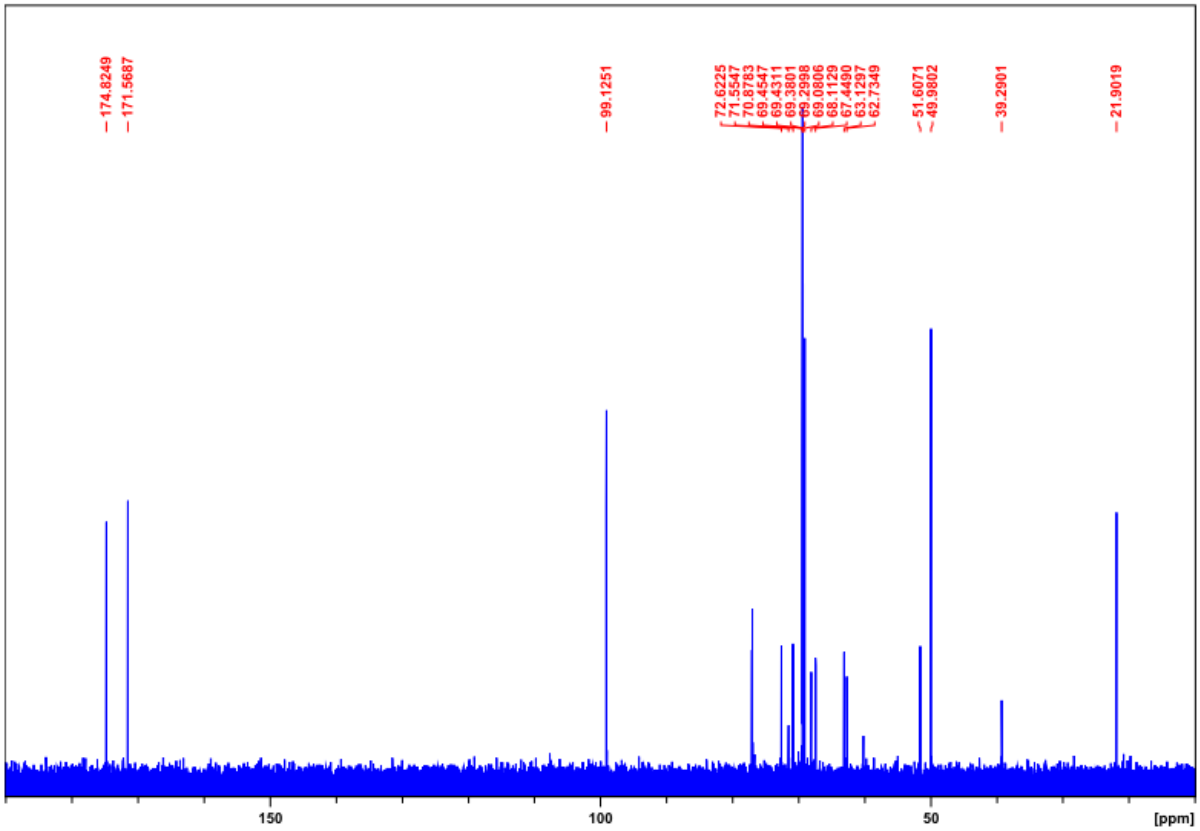

^{1}H-NMR of **AcSia8** (300 MHz, $CDCl_3$):

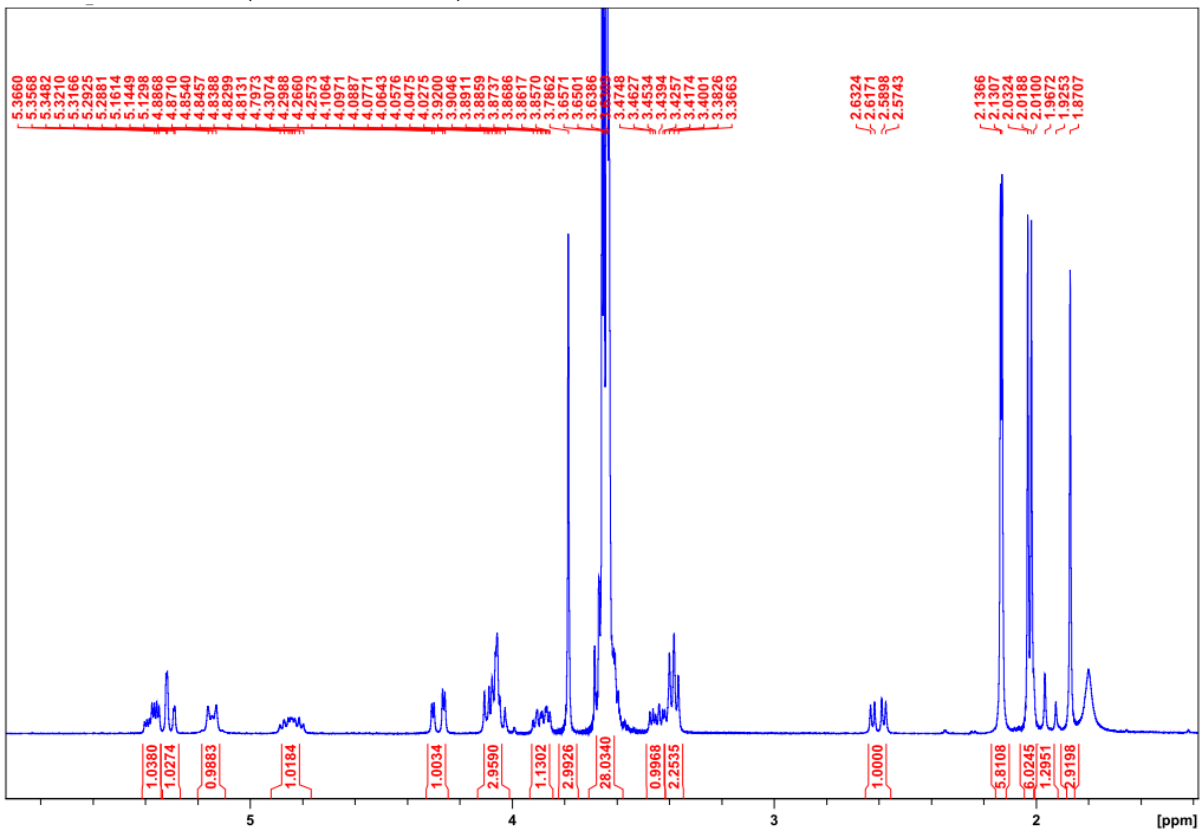

^{13}C-NMR of **AcSia8** (75 MHz, $CDCl_3$):

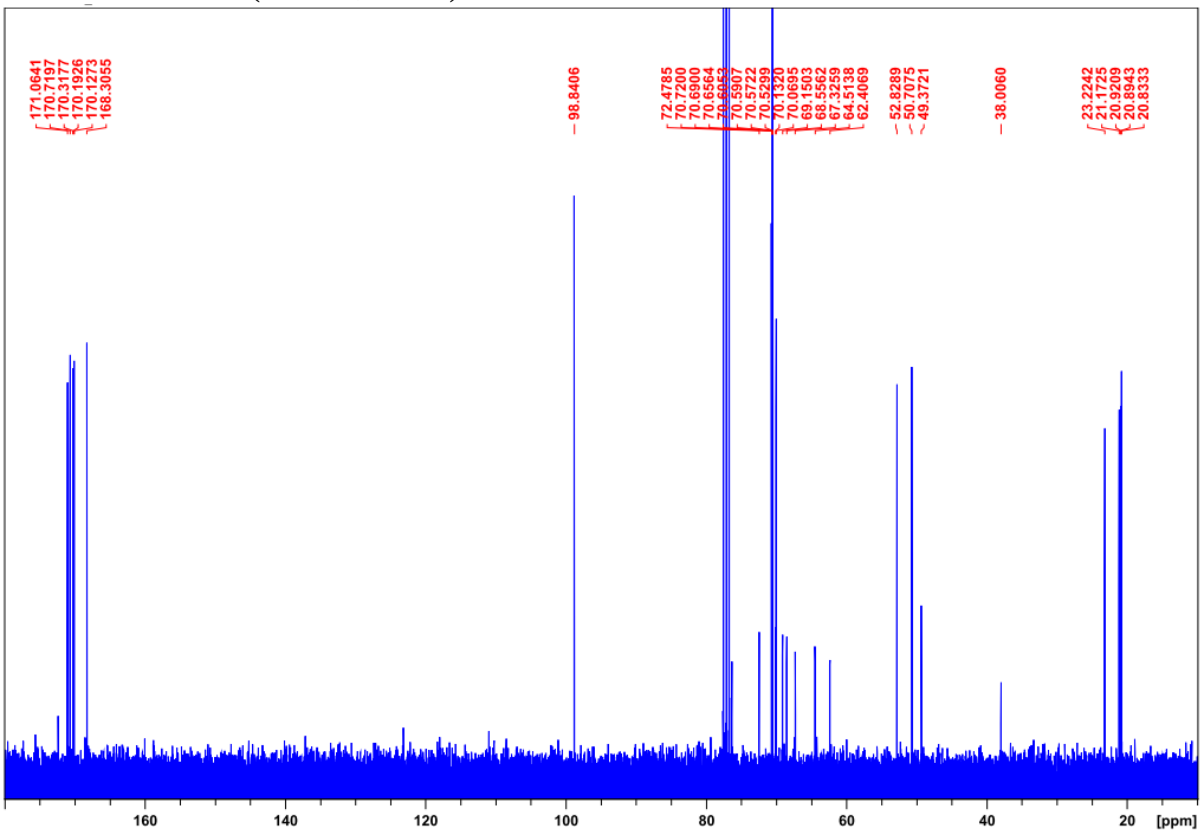

^{1}H-NMR of **Sia8** (300 MHz, D_2O):

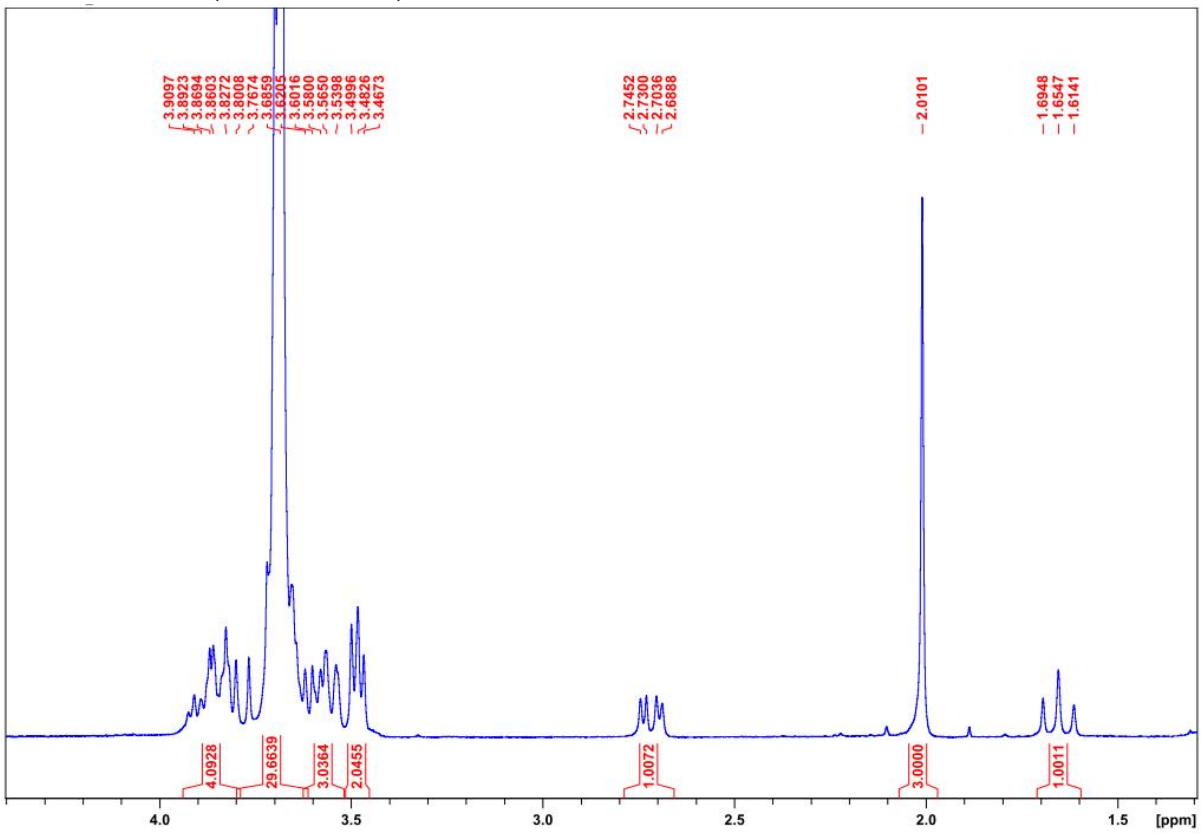

^{13}C-NMR of **Sia8** (150 MHz, D_2O):

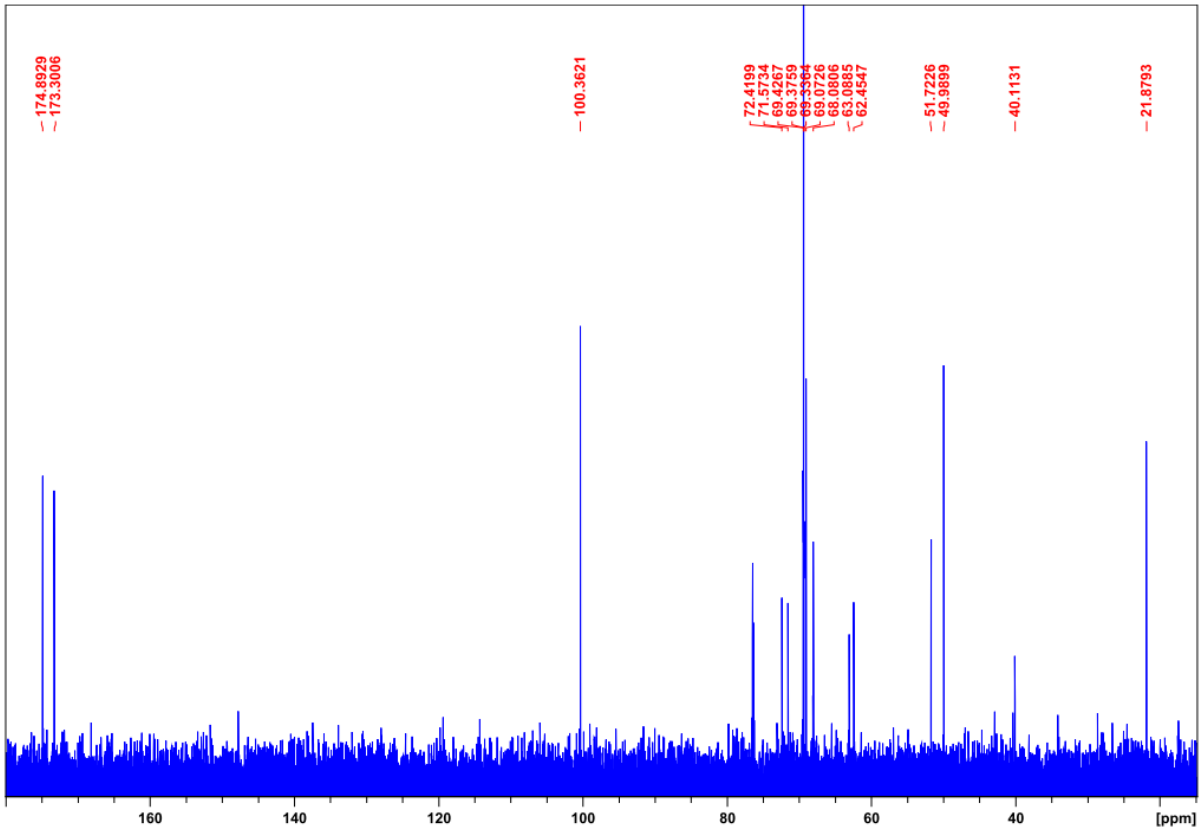

6 References

33. Fulmer, G.R. et al. NMR chemical shifts of trace impurities: common laboratory solvents, organics, and gases in deuterated solvents relevant to the organometallic chemist. *Organometallics* **29,** 2176–2179 (2010).
34. Pfaendler, H.R. & Weimar, V. Synthesis of racemic ethanolamine plasmalogen. *Synthesis* **1996,** 1345–1349 (1996).
35. Amaral, S.P., Fernandez-Villamarin, M., Correa, J., Riguera, R. & Fernandez-Megia, E. Efficient multigram synthesis of the repeating unit of gallic acid-triethylene glycol dendrimers. *Org. Lett.* **13,** 4522–4525 (2011).
36. Murray, J. et al. Solid phase synthesis of functionalised SAM-forming alkanethiol-oligoethyleneglycols. *J. Mater. Chem. B* **2,** 3741–3744 (2014).
37. Svedhem, S. et al. Synthesis of a series of oligo(ethylene glycol)-terminated alkanethiol amides designed to address structure and stability of biosensing interfaces. *J. Org. Chem.* **66,** 4494–4503 (2001).
38. Zhou, Z. & Fahrni, C.J. A fluorogenic probe for the copper(I)-catalyzed azide−alkyne ligation reaction: modulation of the fluorescence emission via 3(n,π*)−(π,π*) inversion. *J. Am. Chem. Soc.* **126,** 8862-8863 (2004).
39. Saludes, J.P., Sahoo, D. & Monreal, I.A. A facile microwave-assisted protocol for rapid synthesis of N-acetylneuraminic acid congeners. *New J. Chem.* **38,** 507 (2014).
40. Orlova, A.V., Shpirt, A.M., Kulikova, N.Y. & Kononov, L.O. N,N-Diacetylsialyl chloride--a novel readily accessible sialyl donor in reactions with neutral and charged nucleophiles in the absence of a promoter. *Carbohydr. Res.* **345,** 721–730 (2010).
41. Weïwer, M., Chen, C.-C., Kemp, M.M. & Linhardt, R.J. Synthesis and biological evaluation of non-hydrolyzable 1,2,3-triazole-linked sialic acid derivatives as neuraminidase inhibitors. *Eur. J. Org. Chem.* **2009,** 2611–2620 (2009).
42. Machida, T., Lang, K., Xue, L., Chin, J.W. & Winssinger, N. Site-specific glycoconjugation of protein via bioorthogonal tetrazine cycloaddition with a genetically encoded trans-cyclooctene or bicyclononyne. *Bioconjugate Chem.* **26,** 802–806 (2015).
43. Dowlut, M., Hall, D.G. & Hindsgaul, O. Investigation of nonspecific effects of different dyes in the screening of labeled carbohydrates against immobilized proteins. *J. Org. Chem.* **70,** 9809–9813 (2005).
44. Pujol, A.M. et al. A sulfur tripod glycoconjugate that releases a high-affinity copper chelator in hepatocytes. *Angew. Chem. Int. Ed.* **51,** 7445–7448 (2012).
45. Rensen, P.C.N., van Leeuwen, S.H., Sliedregt, L.A.J.M., van Berkel, T.J.C. & Biessen, E.A.L. Design and synthesis of novel N-acetylgalactosamine-terminated glycolipids for targeting of lipoproteins to the hepatic asialoglycoprotein receptor. *J. Med. Chem.* **47,** 5798–5808 (2004).
46. Shevchenko, A., Tomas, H., Havli, J., Olsen, J.V. & Mann, M. In-gel digestion for mass spectrometric characterization of proteins and proteomes. *Nat. Protoc.* **1,** 2856–2860 (2007).
47. Hoesl M. G. et al. Lipase congeners designed by genetic code engineering. *ChemCatChem* **3**, 213–221 (2011).
48. Wiltschi B., Merkel L., Budisa N. Fine tuning the N-terminal residue excision with methionine analogues. *ChemBioChem* **10**, 217–220 (2009).
49. Desselberger, U. Relation of virus particle counts to the hemagglutinating activity of influenza virus suspensions measured by the HA pattern test and by use of the photometric HCU method. *Arch. Virol.* **49,** 365-372 (1975).

50. Cross, G. Hemagglutination inhibition assays. *Semin. Avian. Exot. Pet. Med.* **11,** 15-18 (2002).
51. Bhatia, S. et al. Linear polysialoside outperforms dendritic analogs for inhibition of influenza virus infection in vitro and in vivo. *Biomaterials* **138,** 22-34 (2017).
52. Berg, J. et al. Tyk2 as a target for immune regulation in human viral/bacterial pneumonia. *Eur. Respir. J.* **50** (2017).
53. Hocke, A.C. et al. Emerging human middle east respiratory syndrome coronavirus causes widespread infection and alveolar damage in human lungs. *Am. J. Respir. Crit. Care Med.* **188,** 882-886 (2013).
54. Weinheimer, V.K. et al. Influenza A viruses target type II pneumocytes in the human lung. *J. Infect. Dis.* **206,** 1685-1694 (2012).
55. Branston, S. D., Wright, J. and Keshavarz-Moore, E., A non-chromatographic method for the removal of endotoxins from bacteriophages. *Biotechnol. Bioeng.*, **112,** 1714-1719 (2015).
56. Liese, S. & Netz, R.R. Quantitative prediction of multivalent ligand–receptor binding affinities for influenza, cholera, and anthrax inhibition. *ACS Nano* **12**, 4140-4147 (2018).
57. Vonnemann, J. et al. Size dependence of steric shielding and multivalency effects for globular binding inhibitors. *J. Am. Chem. Soc.* **137,** 2572–2579 (2015).
58. Li, S. et al. pH-Controlled two-step uncoating of influenza virus. *Biophys. J.* **106**, 1447–1456 (2014).
59. Wasilewski, S., Calder, L.J., Grant, T. & Rosenthal, P.B. Distribution of surface glycoproteins on influenza A virus determined by electron cryotomography. *Vaccine* **30**, 7368–7373 (2012).
60. Sieben, C. et al. Influenza virus binds its host cell using multiple dynamic interactions. *Proc. Natl. Acad. Sci. U. S. A.* **109**, 13626–13631 (2012).
61. van der Spoel, D. et al. GROMACS: fast, flexible, and free. *J. Comput. Chem.* **26,** 1701–1718 (2005).
62. Bussi, G., Donadio, D. & Parrinello, M. Canonical sampling through velocity rescaling. *J. Chem. Phys.* **126,** 14101 (2007).
63. Parrinello, M. & Rahman, A. Polymorphic transitions in single crystals: A new molecular dynamics method. *J. Appl. Phys.* **52,** 7182–7190 (1981).
64. Darden, T., York, D. & Pedersen, L. Particle mesh Ewald: An Nlog(N) method for Ewald sums in large systems. *J. Chem. Phys.* **98,** 10089–10092 (1993).
65. Essmann, U., Perera, L., Berkowitz, M.L., Darden, T., Lee H. & Pedersen, L. Particle mesh Ewald: A smooth particle mesh ewald potential. *J. Chem. Phys.* **103,** 8577–8592 (1995).
66. Hess, B., Bekker, H., Berendsen, H.J.C., & Fraaije, J.G.E.M. LINCS: A linear constraint solver for molecuar simulations. *J. Comp. Chem.* **18,** 1463–1472 (1997).
67. Jorgensen, J., Chandrasekhar, J.D., Madura, R.W., Impey, R.W. & Klein, M.L. Comparison of simple potential functions for simulating liquid water. *J. Chem. Phys.* **79,** 926–935 (1983).
68. Vorobyov, I. et al. Additive and classical drude polarizable force fields for linear and cyclic ethers. *J. Chem. Theory Comput.* **3,** 1120–1133 (2007).
69. Lee, H., Venable, R.M., MacKerell, A.D. & Pastor, R.W. Molecular dynamics studies of polyethylene oxide and polyethylene glycol: hydrodynamic radius and shape anisotropy. *Biophys. J.* **95,** 1590–1599 (2008).
70. Guvench, O., Mallajosyula, S.S., Raman, E.P., Hatcher, E., Vanommeslaeghe, K., Foster, T. J., Jamison, F.W. & MacKerell, A.D.Jr. CHARMM Additive All-Atom

Force Field for Carbohydrate Derivatives and Its Utility in Polysaccharide and Carbohydrate-Protein Modeling. *J. Chem. Theory Comput.* **7,** 3162–3180 (2011).
71. Hanwell, M.D., Curtis, D.E., Lonie, D.C., Vandermeersch, T., Zurek, E. & Hutchison, G.R. Avogadro: An advanced semantic chemical editor, visualization, and analysis platform. *J. Cheminformatics.* **4**:7 (2012).